FINAL PROGRESS REPORT

Project Title: Determination of Basic Structure-Property Relations for Processing and Modeling in Advanced Nuclear Fuel: Microstructure Evolution and Mechanical Properties

Coverage Period: April 30, 2005 through December 15, 2008

Date of Report: March 1, 2009

Recipient: Arizona State University

Award Number: DE-FC07-05ID14654

Contact(s):   Ken Osborne, osbornkk@id.doe.gov, Dr. Pedro Peralta, 480-965-2894, pperalta@asu.edu

Project Team: Kirk Wheeler, Arizona State University, kirk.wheeler@asu.edu
Manuel Parra Garcia, Arizona State University, manuel.parra@asu.edu
Dr. Kenneth J. McClellan, Los Alamos National Laboratory, kmcclellan@lanl.gov
Dr. Jeremy Mitchell, Los Alamos National Laboratory, jeremy@lanl.gov

Project Objective: The project objective is to study structure-property relations in solid solutions of nitrides and oxides with surrogate elements to simulate the behavior of fuels of inert matrix fuels of interest to the Advanced Fuel Cycle Initiative (AFCI), with emphasis in zirconium-based materials. Work with actual fuels will be carried out in parallel in collaboration with Los Alamos National Laboratory (LANL). Three key aspects will be explored: microstructure characterization through measurement of global texture evolution and local crystallographic variations using Electron Backscattering Diffraction (EBSD); determination of mechanical properties, including fracture toughness, quasi-static compression strength, and hardness, as functions of load and temperature, and, finally, development of structure-property relations to describe mechanical behavior of the fuels based on experimental data. Materials tested will be characterized to identify the mechanisms of deformation and fracture and their relationship to microstructure and its evolution. New aspects of this research are the inclusion of crystallographic information into the evaluation of fuel performance and the incorporation of statistical variations of microstructural variables into simplified models of mechanical behavior of fuels that account explicitly for these variations. The work is expected to provide insight into processing conditions leading to better fuel performance and structural reliability during manufacturing and service, as well as providing a simplified testing model for future fuel production.

Background: The development and certification of new fuels under the Advanced Fuel Cycle Initiative (AFCI) is challenging because resources are no longer available for extensive experimental characterization of nuclear fuels before and after irradiation. In particular, Post-Irradiation Examination (PIE) is extremely expensive and the needed infrastructure to perform irradiation testing at adequate fluxes is inadequate in the US. Therefore, fuel development must rely heavily on modeling to predict performance, which must be based on physically based mechanisms, rather than empirical relationships derived from curve fitting of experimental data. A suitable strategy is to carry out experimental work in relevant surrogate materials, particularly in the case of inert matrix fuels, where less experimental characterization is currently available.

Milestones: October 2004-September 2005:
Overall Goal: Development of processing procedures to fabricate pellets of solid solutions of nitride and oxide surrogates of inert matrix fuels and characterization of their microstructures and room temperature mechanical properties.

Goal: Establish appropriate surrogates for Pu in order to fabricate nitride and oxide surrogate pellets using expertise available at LANL and attempt fabrication of samples.
Work towards achievement of goal: An investigation was initiated into appropriate PuN surrogates. Cerium nitride was closely examined as a strong possibility, given Cerium's well known role as a surrogate for Pu in Plutonium oxides; however, it was found that high purity CeN powder was not readily available through regular commercial vendors. In addition, CeN in powder form was found to be unstable when exposed to air, since it has a strong tendency for oxidation, which makes it a fire hazard. Emphasis has been placed on fine-tuning the processing of ZrN pellets and the examination of incipient plasticity on this material, which could affect processing of solid solutions of zirconium and actinide nitrides significantly.

Goal: Improve on manufacturing procedures for surrogate pellets and establish quality of material produced via microstructural characterization.
Work towards achievement of goal: Initial test samples fabricated with milled ZrN powders having a wide particle size distribution had low sample density and inconsistent pore size distribution, while samples made of powders having a narrower particle size distribution and a smaller average size, 5 micron, had increased density and a much more uniform pore distribution. Examination of the microstructure of ZrN pellets sintered at two different temperatures (1600 °C and 1300 °C) revealed substantial differences. The pellet sintered at higher temperature had a uniform grain structure, due to the active mass transport, while the samples sintered at lower temperatures had a non-uniform microstructure. Both samples displayed a lognormal pore distribution dominated by small pores (d ≤ 1 μm), but the sample sintered at higher

temperatures had a larger fraction of small pores than the sample sintered at lower temperatures, as shown in Fig. 1.
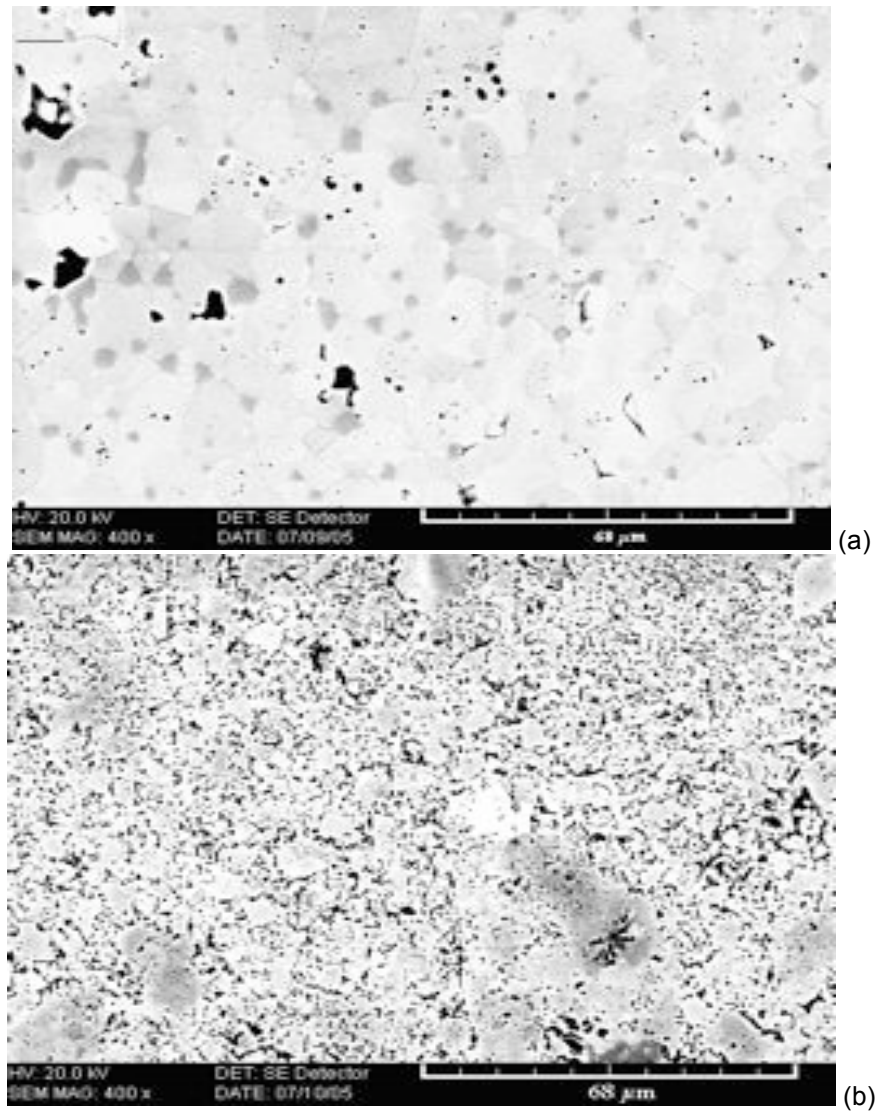

(a)

(b)

Fig. 1: Microstructure in ZrN sintered at (a) 1600°C, and (b) at 1300 °C

A change in crystallographic texture was noticed between the "green" samples (before sintering) and the sintered samples, where a tendency for texture to develop <111> components.   This texture evolution is consistent with the presence of dislocation slip.   A series of nanoindentation experiments were carried out to examine the dislocation activity on the surface of ZrN. It was found that the load-penetration curves from nano-indentation on the polished surface displayed a displacement jump of 31±3 nm at an average load of 1100±200 µN. The presence of this jump indicated a permanent indentation in the sample, whereas loads below the critical value to produce the jump resulted in elastic behavior that followed the well-known Hertzian behavior.

Goals: Optimize manufacturing process and establish microstructural evolution during sintering.

Measure mechanical properties of surrogate pellets at room temperature and establish their relationship to microstructure. Obtain correlations between hardness and other properties.

Work towards achievement of goal: The effects of sintering conditions on the microstructural evolution and mechanical properties of sintered ZrN pellets, as surrogates for actinide fuels, have been studied. Samples were sintered at either 1600°C or 1300°C in Argon or Nitrogen environments. Argon sintered samples were found to have a more developed equiaxed grain structure and more well-defined grain boundaries than samples sintered in nitrogen at the same temperature, which had a composite structure consisting of small dense regions of grain growth surrounded by weakly bonded particles exhibiting very little grain nucleation. The dense regions of grain growth found in Nitrogen sintered samples looked similar in shape and porosity concentration as the grain structure of the Argon sintered samples, except that the grains in these dense regions were much smaller. As a result of this difference in grain structure, the porosity of Argon sintered samples was more uniformly distributed, located both inside grains and at grain boundaries, as compared to the irregularities in porosity distribution caused by the bimodal microstructure in Nitrogen sintered samples, as shown in Figures 2 and 3.
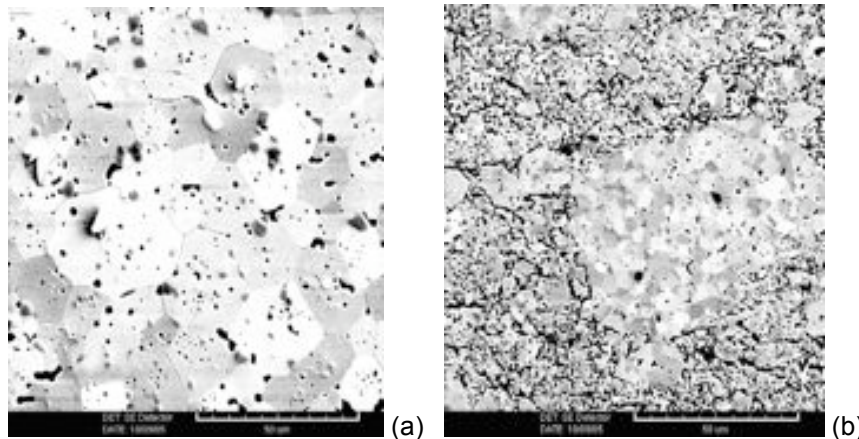

(a)   (b)

Fig. 2: Typical microstructure of samples sintered at 1600 °C. (a) Argon atmosphere, (b) Nitrogen atmosphere. Scale bar is 50 µm in both images.
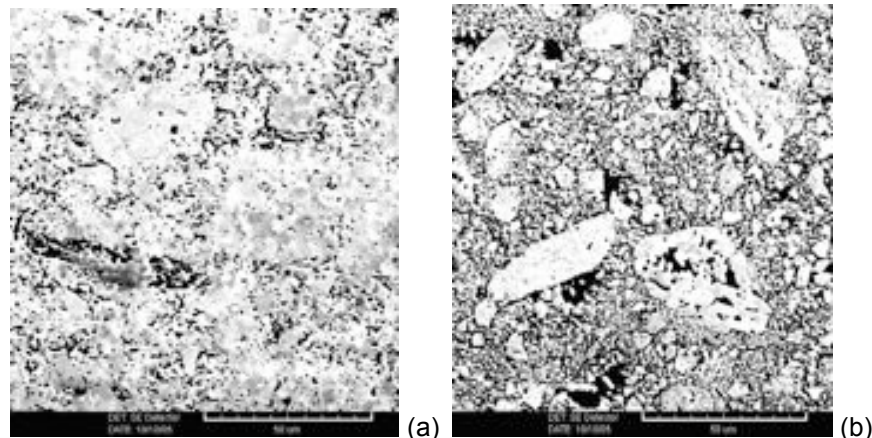
(a)   (b)

Fig. 3: Typical microstructure of samples sintered at 1300 °C. (a) Argon atmosphere, (b) Nitrogen atmosphere. Scale bar is 50 µm in both images.

Samples sintered at either 1600°C or 1300°C in Argon or Nitrogen environments with and without 6% Hydrogen were also studied. Samples sintered with the addition of Hydrogen had lower average hardness compared to identically prepared samples sintered without it (see Fig. 4), due to an increase in porosity and a clear tendency for intergranular fracture.
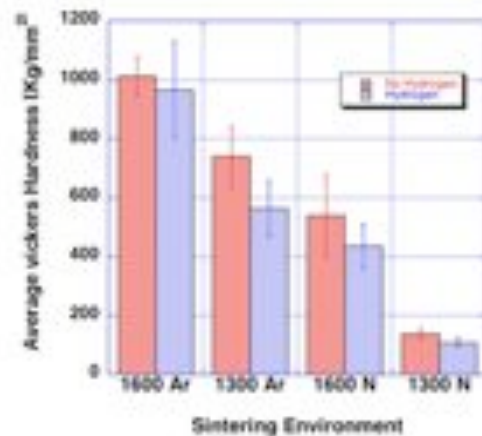

Fig. 4: *Vickers Hardness as a function of Sintering Temperature and Atmosphere*

Microstructural maps obtained via EBSD and crystallographic texture measurements indicate that the grain growth kinetics was different between both environments at the same temperature, as can be seen in Fig. 5. In this figure, the Inverse Pole Figure (IPF) maps are such that the color of a grain is related to a crystallographic direction in the grain that is parallel to a certain physical direction, in this case the out-of-plane direction (normal to the plane of the sample). The difference in sintering kinetics could be due to a possible atomic solubility and diffusion associated with Nitrogen gas during sintering and the presence of point defects due to deviations from stoichiometry.
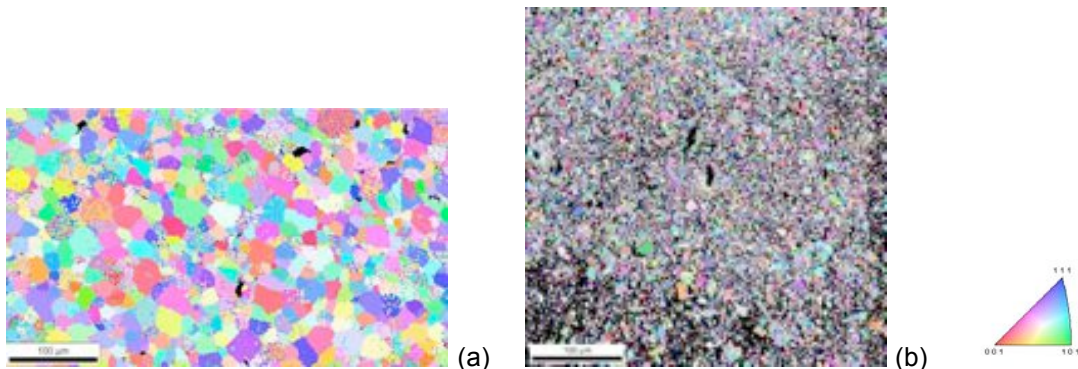
5

Fig. 5: Inverse pole figure (IPF) maps for (a) 1600 °C Ar and (b) 1600 °C N. Scale bar=100 µm in both figures.

The crystallographic texture of Argon sintered samples displayed a sharper texture, which is consistent with the presence of larger grains, while N_2 sintered samples exhibit a smoother texture due to the presence of fine particles and smaller grains, as shown in Fig. 6.
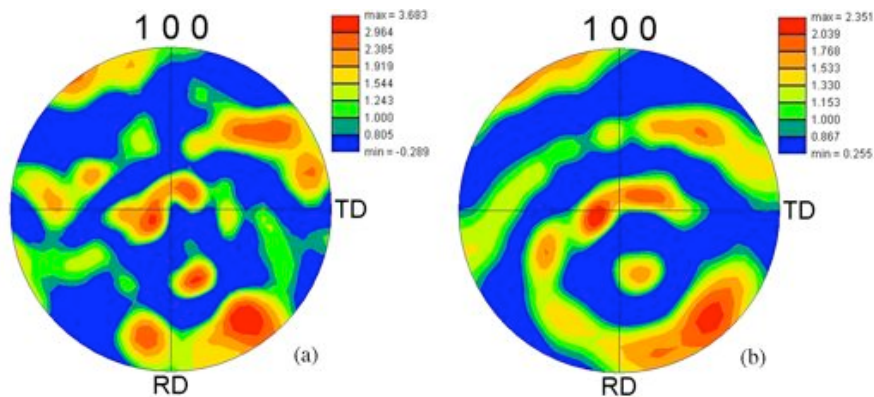

Fig. 6: {001} pole figures. (a) 1600 °C Ar. (b) 1600 °C N.

Processing parameters leading to optimum microstructures were narrowed down to an Ar sintering atmosphere with temperatures between 1300°C and 1600°C, depending on the desired final density. Electron Backscatter Diffraction analysis indicated that samples sintered at 1600°C in an Argon environment had a more uniform grain size as compared to samples sintered at the same temperature in an Ar-6%H_2 environment. In contrast, the Ar-6%H_2 sample had a greater number of high angle grain boundaries, which have been shown to be intrinsically weaker in ZrN in this work, since cracks around indents had a clear tendency to follow high angle grain boundaries (see Figures 7 and 8). This is likely to be the case in actinide nitrides as well. This suggests that increasing the fraction of low angle boundaries could lead to improvements in fracture behavior in nitride fuels.
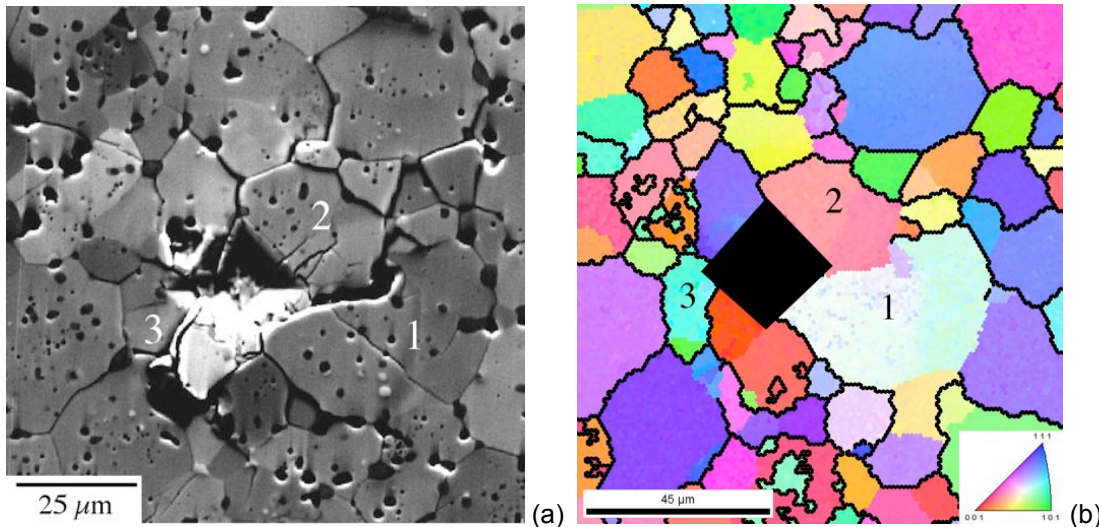
Fig. 7: *"Typical" indent in a sample sintered at 1600 °C in Ar. (a) SEM image, (b) Inverse pole figure. The scale bar in (b) is 45 µm long. Black lines indicate boundaries with a misorientation larger than 30°.*

Fig. 8: *"Typical" indent in a sample sintered at 1600 °C in Ar-6%H. (a) SEM image, (b) Inverse pole figure. The scale bar in (b) is 45 µm long. Black lines indicate boundaries with a misorientation larger than 30°.*
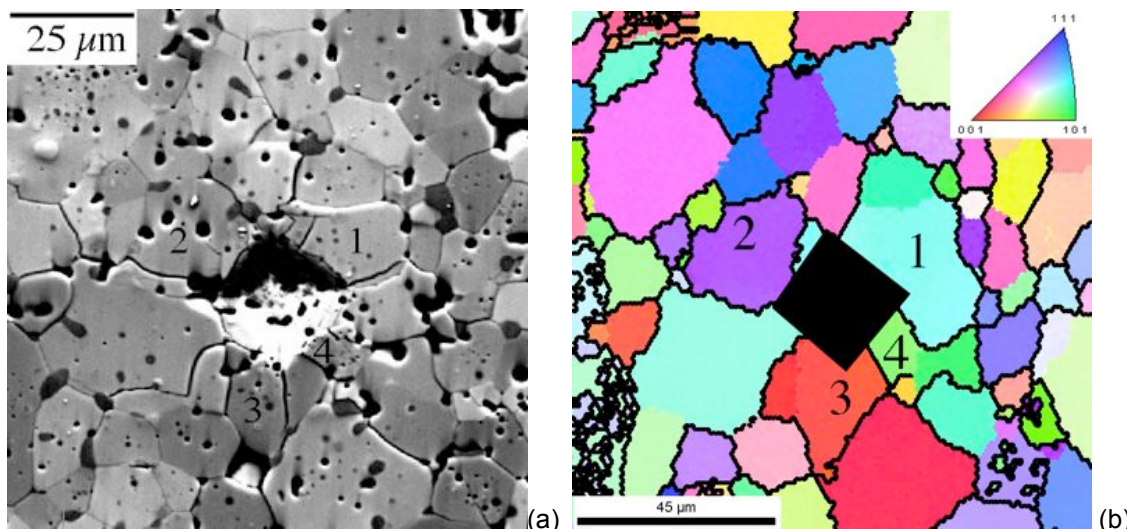
October 2005-September 2006:
Overall Goals: Establish mechanical behavior at intermediate temperatures and characterize microstructure evolution of surrogates under thermal and mechanical loads as well as microstructure of actual fuels.
Establish structure-property relations and formulate a simplified two-dimensional model of structural fuel behavior.

Goal: Formulate mechanisms of deformation and fracture and initiate explicit model of microstructures.
Work towards achievement of goal: A two-dimensional model of a low density ZrN pellet was constructed using finite elements that accounted

for the actual microstructure of the pellet. This microstructure was assumed to consist of three different phases: dense clusters, porous matrix and large pores. Methodologies were developed to identify each phase using SEM micrographs and geometric and crystallographic orientation variability was identified using EBSD mapping and this information was converted into a finite element mesh. A 2D model was used to obtain effective Young's modulus along two perpendicular directions. As expected, pore shape and orientation were found to lead to measurable anisotropy in the value of effective Young's modulus and stress concentrations were found at the interfaces between pores, clusters and the porous matrix, which indicates that these locations are the most likely sites for failure during loading, as shown in Fig. 9. This study illustrates the importance of accounting for actual microstructure on fuel modeling and simulation.
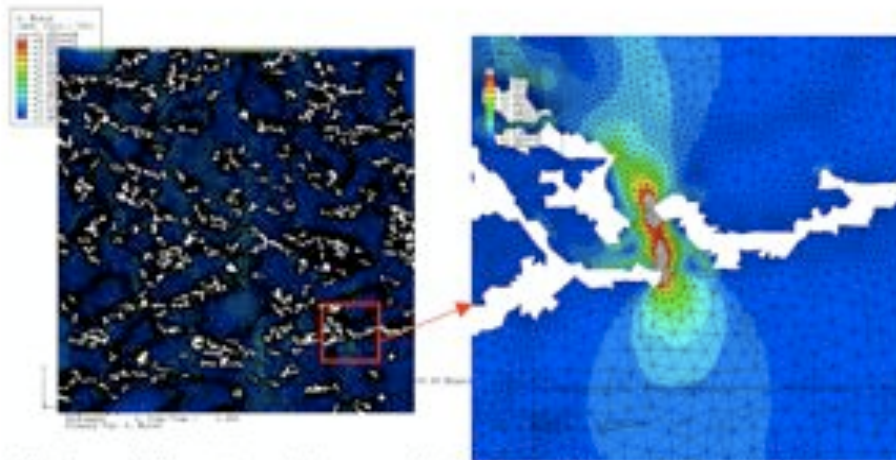

Fig. 9: von Mises stress in the sample. (a) General view; (b) Detail of local maximum.

A 2D model of a high density ZrN pellet was constructed using finite elements that accounted for the actual microstructure of the pellet (Fig. 10). An EBSD map was processed to create a model that accounts for both geometric and crystallographic variability of the microstructure, as well as anisotropy of the mechanical properties at the microscale. Methodologies were developed to assign each grain a certain orientation and to import the geometry into a finite element mesh.
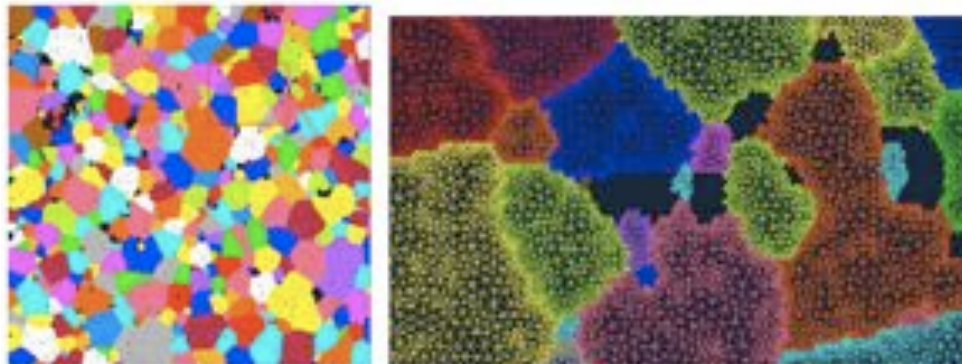

Fig. 10. Mesh of Sample sintered at 1600°C with each grain assigned a different material.

It was determined that the shape and variability of pores along with preferential crystallographic orientation of the grains can lead to anisotropy in the value of the effective Young's modulus. These simulations showed that high stress concentrations in high-density samples are found at the interfaces between grains and intergranular pores (Fig. 11). In low-density samples, stresses showed higher variability and were affected by local pore geometry and the presence of interfaces among the different phases considered, (dense clusters, low density porous matrix and voids).
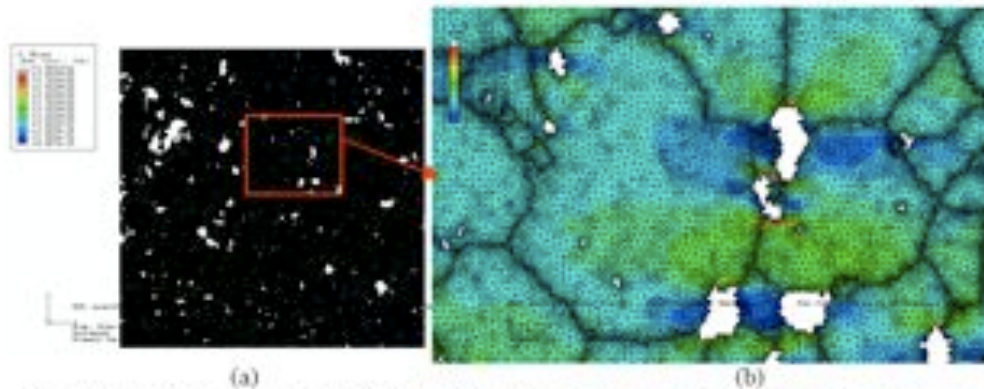

Fig. 11. Von Mises stress in the high density sample. (a) General view; (b) Local maximum.

In order to address the behavior of actual inert matrix fuels, which in nitrides would consist of at least a basic solid solution of PuN and ZrN, pellets having smaller diameters, ~4mm compared to the ~12mm diameter of previous samples, were fabricated from solid solutions of ZrN and TiN and were sintered in an Argon environment at 1375°C, 1475°C and 1600°C, based on sintering densification curves that were developed during this project. The (Zr,Ti)N samples were fabricated because the relative atomic size mismatch between Zr and Ti is similar to that between Pu and Zr, so these pellets are expected to lead to further insights into the processing and properties of solid solutions of actinide and transition metal nitrides. No significant sample size effects were noticed based on similarity of sample density, grain size and pore distribution of each of the different ZrN samples. The microstructure of the (Zr,Ti)N samples was very different compared to pure ZrN samples, as they displayed significantly reduced density and smaller average grain size under similar sintering conditions, as shown in Fig. 12.
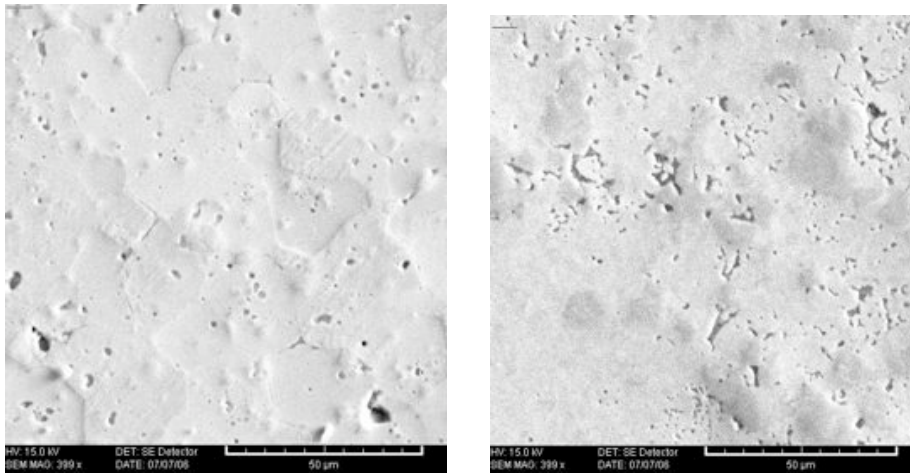
Fig. 12: Typical microstructure of (a) ZrN, 1600°C. (b) (Zr,Ti)N, 1600 °C. Scale bar=50 μm in both figures.

Electron microscopy indicates that "solid solution" pellets did not form a one-phase solid solution, but rather two phases were present, one rich in Zr and the other rich in Ti, although the distribution was more uniform in samples sintered at high temperatures (see Fig. 13). This is attributed to a reduction in kinetics due to the mismatch in atomic size between Zr and Ti.
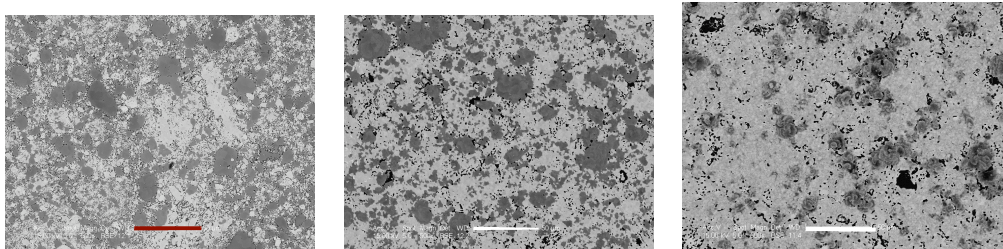

Fig. 13: Backscattered electron images of solid solution (Zr,Ti)N pellets: (a) 1375°C; (b) 1475°C; (c) 1600°C. Scale bar is 50μm long in all images.

Uniaxial compression tests showed that solid solution pellets had a higher specific strength compared to pure ZrN pellets, despite the fact that solid solution pellets had lower densities,a s shown in Fig. 14.
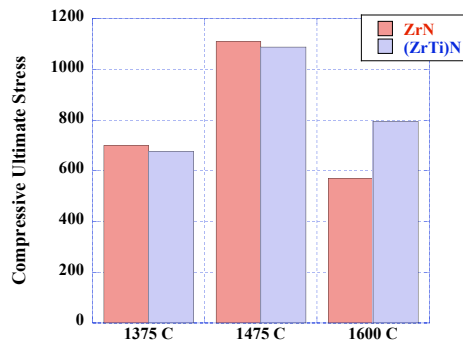
Fig 14: *(a) Ultimate compressive strength (in MPa) for pure ZrN and solid solution pellets as a function of sintering temperature.*

The increased specific strength of the 'solid solution' pellets was attributed to smaller grain size and increased porosity, since the larger number of grain boundaries and pores in the solid solution will provide sites for energy dissipation allowing for more damage accumulation before catastrophic failure. Fracture surfaces were examined after compression tests, as shown in Fig. 15.
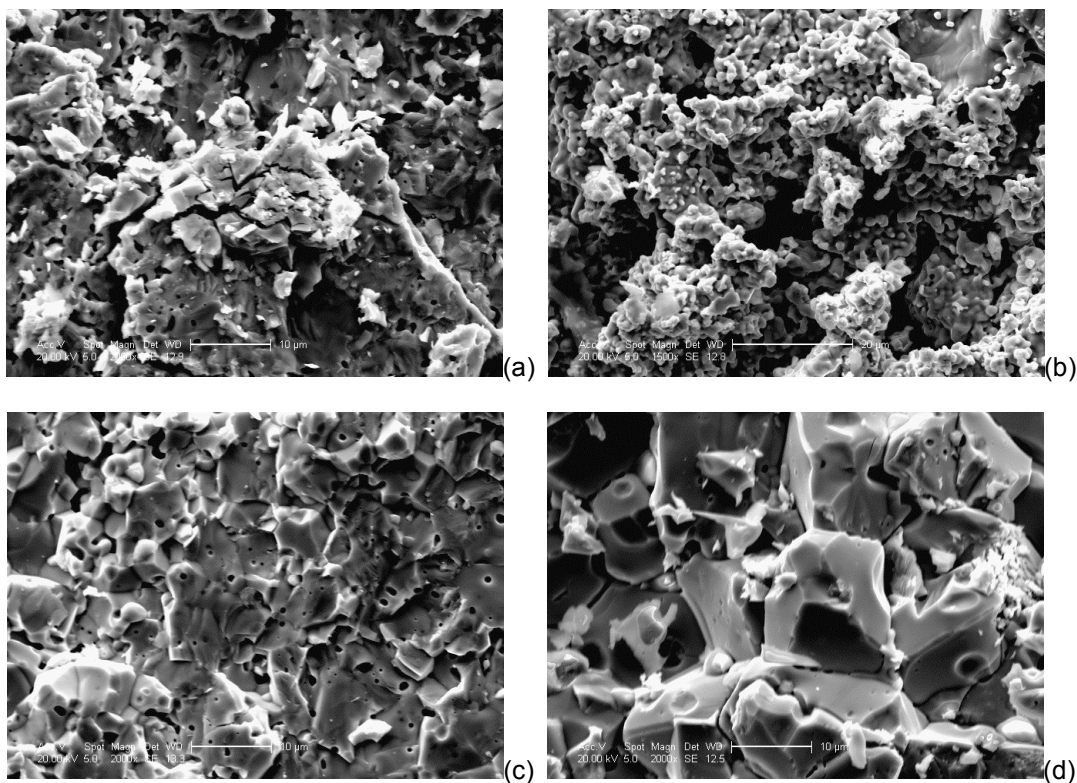

Fig. 15: *Fracture surface of: (a) (Zr,Ti)N, 1475℃ 2000x, 10 μm scale; (b) (Zr,Ti)N, 1600℃ 1500x, 20 μm scale; (c) ZrN, 1475℃ 2000x, 10 μm scale; (d) ZrN, 1600℃ 2000x, 10 μm*

Composition maps of the fracture surfaces using Energy Dispersion Spectroscopy (EDS), indicated a tendency for fracture along the Zr rich phase, as shown in Fig. 16.
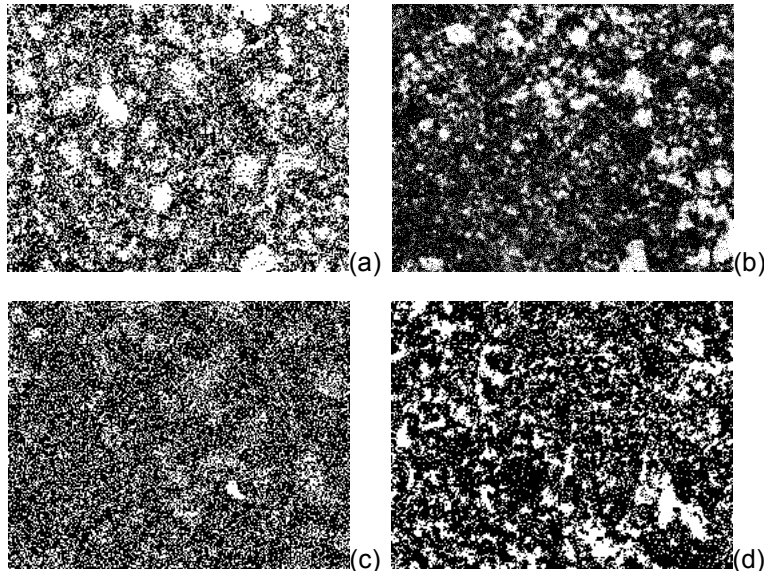

Fig. 16: Composition maps on fracture surfaces of solid solution pellets obtained using EDS. Zr distribution (black) in (Zr,Ti)N samples: (a) 1375°C smooth surface; (b) 1375°C fracture surface; (c) 1600°C smooth surface; (d) 1600°C fracture surface.

Goal: Formulate mechanisms of deformation and fracture and continue formulation of explicit model of microstructures.

Work towards achievement of goal: Microstructurally explicit models were refined to improve on the estimates of effective Young's moduli along different directions. The effective Modulus of Elasticity, E_{eff}, of the sample decreased with respect to the value for monolithic ZrN, as expected. The 2-D models account for variability due to the orientation of individual grains and the effect of local concentration of porosity; this makes it possible to observe anisotropy on the mechanical behavior of high density sintered nitride fuels and the effect of porosity on effective mechanical properties and failure. An example of the models formulated and the results obtained using those models is shown in Figures 17 and 18.
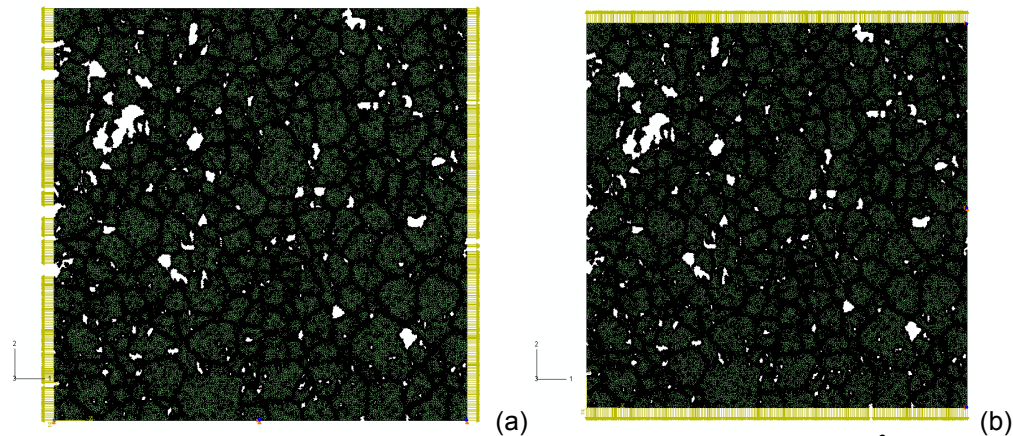
Fig. 17: Finite element models used to determine effective Young's modulus. *(a) 10^6 units of stress in the horizontal direction; (b) 10^6 units of stress in the vertical direction.*
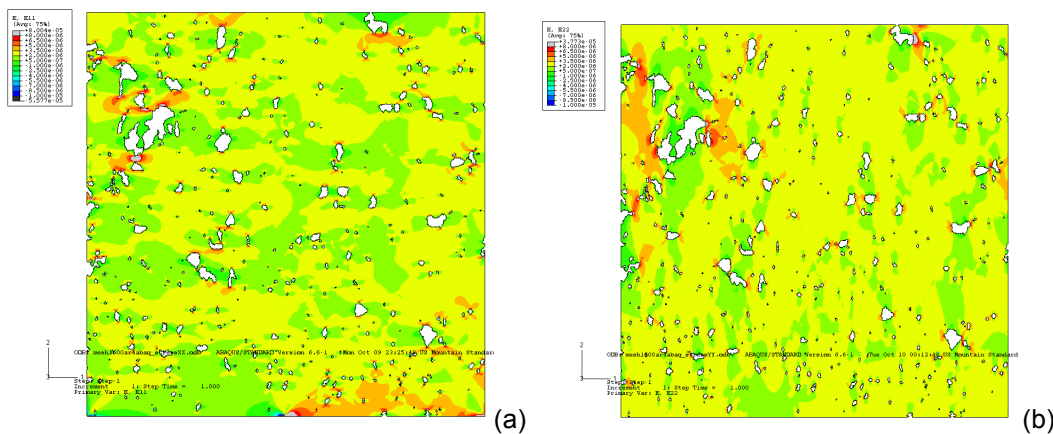
Fig. 18: *(a) Strain distribution generated from loading in the horizontal direction; (b) Strain distribution generated from loading in the vertical direction.*

Regarding other mechanical properties, results of indentation testing showed that hardness values of ZrN and (Zr,Ti)N solid solutions were the lowest at 1375°C sintering temperature, peaked at 1475°C and decreased for pellets sintered at 1600°C, as shown in Fig. 19.

Fig. 19: *Comparison of (a) Hardness and (b) Compressive Strength of ZrN (red) and (Zr,Ti)N (blue) samples sintered at various temperatures.*

October 2006-September 2007:
Overall Goal: Establish mechanical behavior and microstructural evolution of surrogates at high temperatures. Establish structure-property relations and formulate a simplified two-dimensional model of structural fuel behavior.

Goals: Formulate mechanisms of deformation and fracture and initiate explicit model of microstructures.
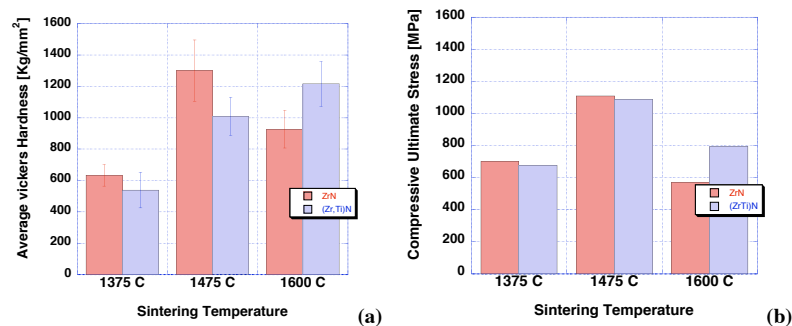Compile all available data needed as input for the model and estimate variability in surrogate pellet structural response via simplified finite element models.
Work towards achievement of goal: A "composite" finite element model of a cylindrical fuel element at its initial stages was developed. The model contained a Representative Volume Element (RVE) that was microstructurally explicit surrounded by homogeneous material and was used to estimate scatter on local stresses in a pellet due to microstructural heterogeneity. This model was used under different boundary conditions and results for a traction boundary value problem, i.e., a pressure applied at the outside boundary, are presented in figure 20.
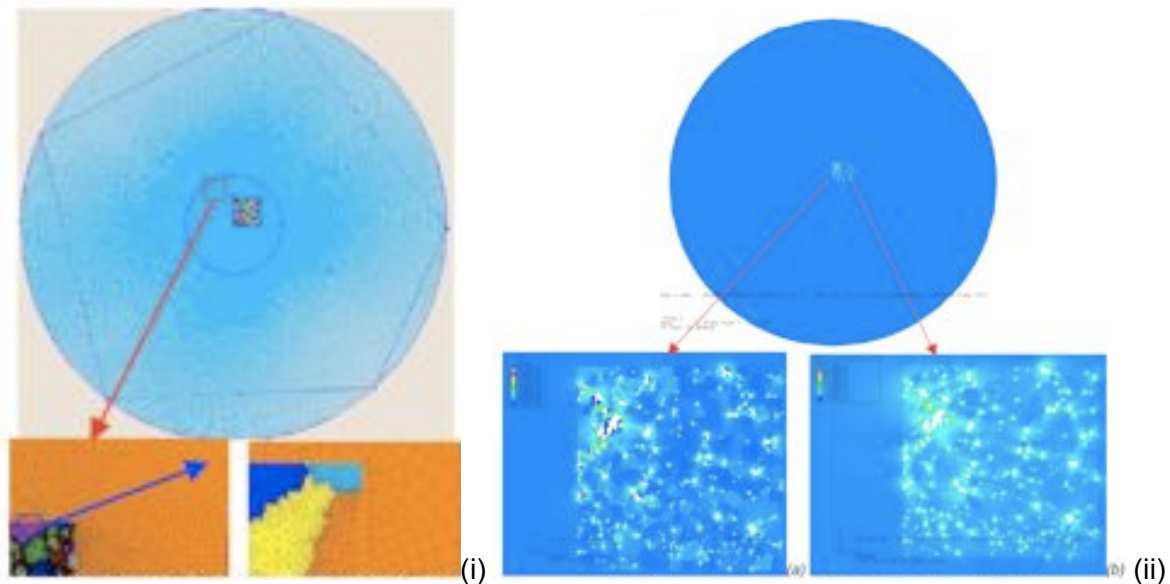
Fig. 20: (i) Finite Element Thermo-mechanical model, (ii) (a) Von Misses stress plot (b) Maximum In-plane principal strain

This boundary condition was meant to mimic the contact pressure resulting from pellet-cladding mechanical interaction. The results indicate that stress indeed concentrates on particular locations in the microstructure, in this case at intergranular porosity. These locations represent possible damage initiation sites. Further work was used examine the scatter on the stress distributions due to both thermal and mechanical loads and will be presented later in this report.

Efforts to perform multi-scale mechanical property characterization on dense ZrN pellets were undertaken, to complement the multi-scale modeling effort. In particular, a technique was developed to mark and locate grains on a sample with a chosen crystallographic orientation using Focused Ion Beam (FIB) micromachining, as shown in Fig. 21. This was done so that nanoindentation tests could be performed in these grains. This allowed evaluating hardness elastic modulus as functions of grain orientation, which in turn provided mechanical property data that could be used in the microstructurally explicit models of the structural behavior of the fuel pellet.

(a)   (b)
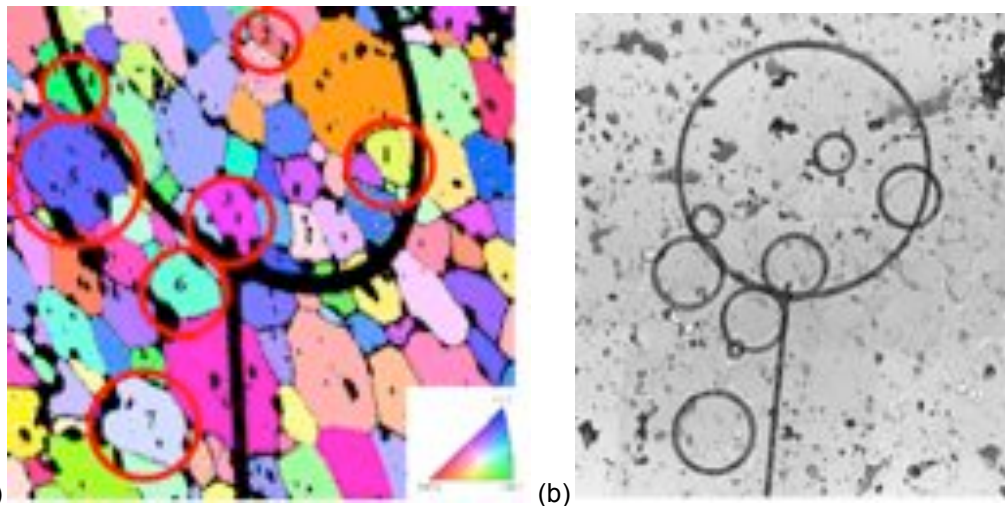
Fig. 21: (a) EBSD image of numbered test grains, (b) Optical microscopy image of sample with fiducial marks isolating desired grains

Efforts on the project were also concentrated on translating the characterization and modeling techniques that were developed for sintered zirconium nitride to oxide materials, particularly zirconium oxide, which is a potential material to be used as a matrix for inert and low fertility fuels and also depleted uranium oxide. Techniques to improve the quality and resolution of EBSD scans were fairly successful on samples of Yttria Stabilized Zirconia (YSZ) made through either conventional sintering or multimode microcrowave (MMMW) techniques. Material for this study was obtained through a collaboration with a D. Folz and D. Clark in Virginia Tech. Grains were fairly small for these samples with averages of about 1.5µm for the MMMW samples and 2 µm for the conventionally sintered (CS) samples, as shown in Fig. 22.

Fig. 22: *IPF maps of YSZ pellets sintered at 1500°C via (a) Conventional Sintering, scale bar = 15µm (b) MMMW Sintering, scale bar = 15µm*

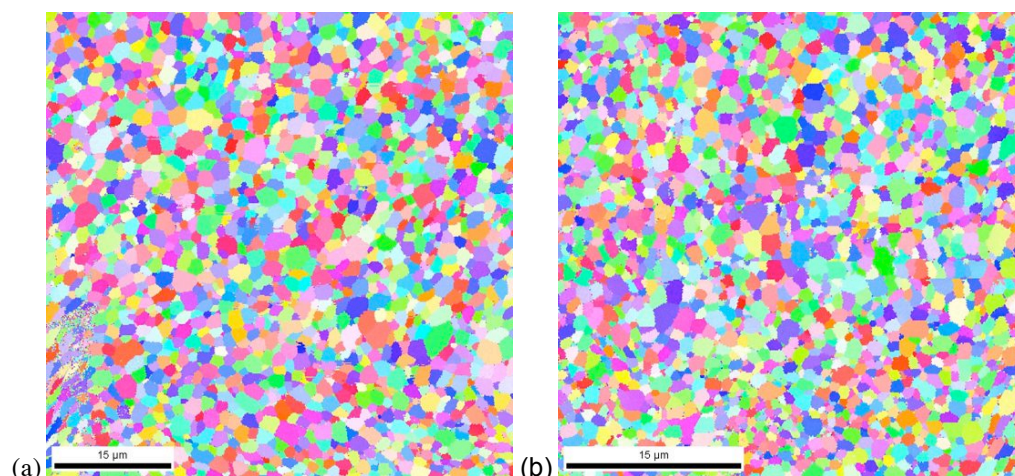In addition, sectioning and polishing techniques were used to create two-dimensional (2D) and three-dimensional (3D) representations of the microstructure of ZrN pellets sintered at 1600°C in Argon atmosphere and YSZ dense pellets sintered at 1500°C using conventional and microwave sintering techniques. The ZrN pellets were characterized using polishing techniques along with EBSD, whereas the YSZ pellets were studied using serial sectioning via FIB milling as well as EBSD. It was found that layers as small as 40 nm could be removed from the non-conductive YSZ samples while maintaining a smooth surface finish.

In addition, the same characterization done in solid solution nitride pellets was extended to YSZ pellets prepared by either conventional sintering techniques or using a mixed mode microwave (MMMW) technique. Furthermore, compression tests at high temperature were performed for all samples. It was found that both ZrN and (Zr,Ti)N samples follow a trend of increasing compressive strength with increasing sintering temperature when tested at 25 °C. The trend is similar when tested at 800°C, except all samples sintered at 1600°C exhibit a reduction of compressive strength. The one exception to these trends was the pure ZrN sample sintered at 1600 °C, which was found to have a relatively low compression strength due to its comparatively larger grain size (~20 µm) and large pores located at grain boundaries. Samples sintered at 1475°C exhibited the greatest compression strength at both 25°C and 800°C. Both samples showed a reduction in compression strength by nearly 50% when tested at 800° (ZrN: 2060 MPa down to ~1000 MPa, (Zr,Ti)N: 1640 MPa down to ~1000 MPa), as shown in Fig. 23.

16
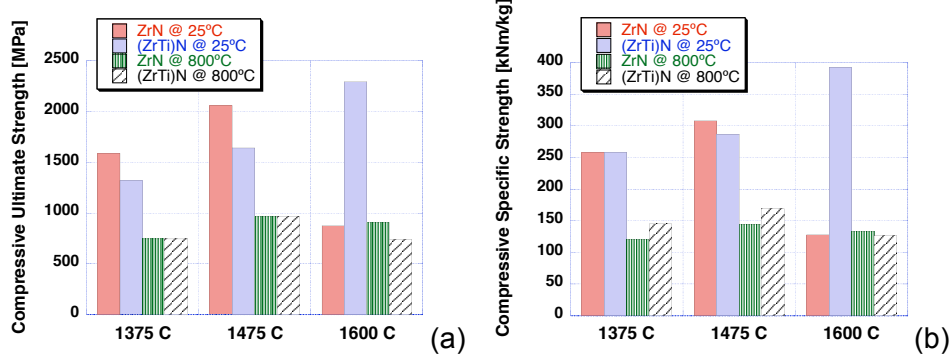
Fig. 23: Comparison of ZrN and (Zr,Ti)N pellets tested at 25°C and 800°C: (a) Ultimate Compressive Strength (b) Specific Compressive Strength

Yttria Stabilized Zirconia (YSZ) samples exhibited the same trend of reduced compression strength at 800°C as the two ZrN based samples (Sintered YSZ: ~1300 MPa down to ~650 MPa, MMMW YSZ: ~1650 MPa down to ~1000 MPa), as shown in Fig. 24.
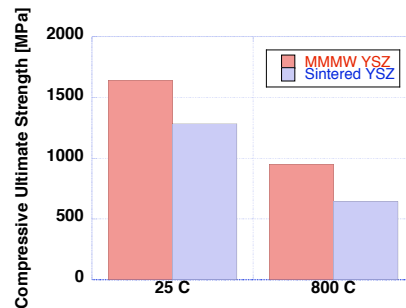
Fig. 24: Ultimate compressive strength comparison between traditionally sintered YSZ and MMMW sintered YSZ tested at 25°C and 800°C

In addition, it was found that the conventionally sintered YSZ samples microstructure consists of submicron grains with very little sintering, i.e., no significant growth and adhesion of powers and little densification, as shown in Fig. 25.
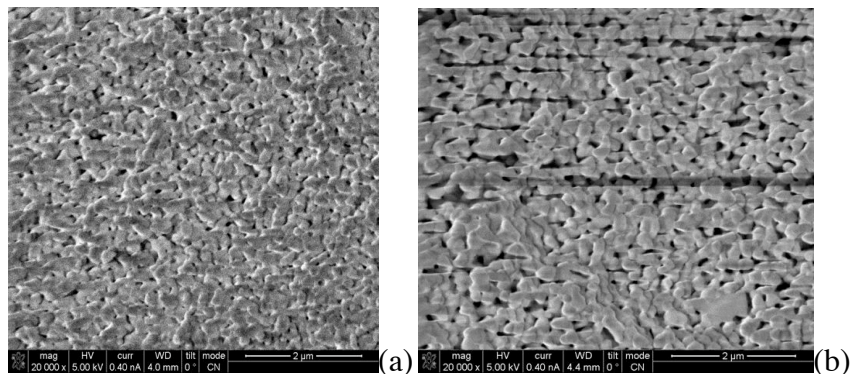
Fig. 25: Compression test fracture surface of sintered YSZ: (a) 25°C, 20000x, 2μm scale; (b) 800°C, 20000x, 2μm scale

The MMMW sample also had very small submicron grains, but displays characteristics of a more complete sintering, i.e., equiaxed grains and densification (see Fig. 26).

(a)   (b)
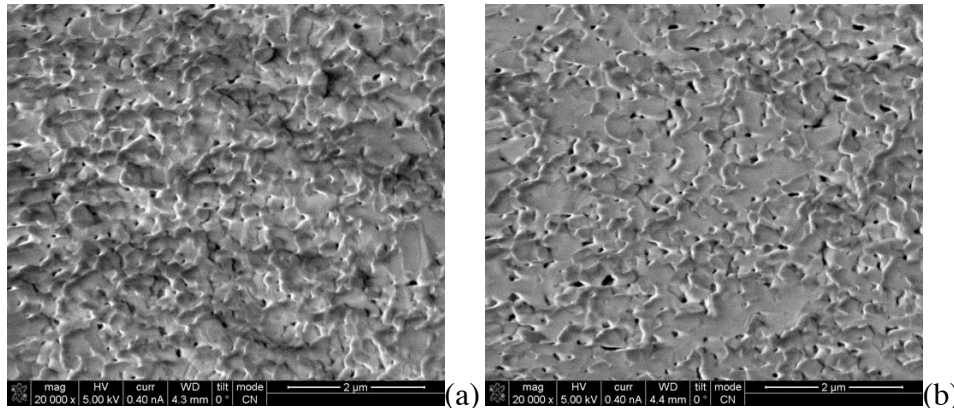
Fig. 26: *Compression test fracture surface of MMMW YSZ: (a) 25°C, 20000x, 2μm scale; (b) 800°C, 20000x, 2μm scale*

October 2007-September 2008:

Goals: Continue formulation of explicit model of microstructures.
Compile all available data needed as input for the model and estimate variability in surrogate pellet structural response via simplified finite element models.
Work towards achievement of goal: A 3-D microstructurally explicit model for ZrN was obtained using 3D Computer Aided Design (CAD) software to simulate stress-strain behavior of a generic microstructural volume element subjected to tensile stress to study critical regions for stress concentration. This model was compared to previous 2-D models and it was found that the highest stress concentrations occur at the grain boundaries, both in the 2D and 3D models, as shown in Fig. 27.
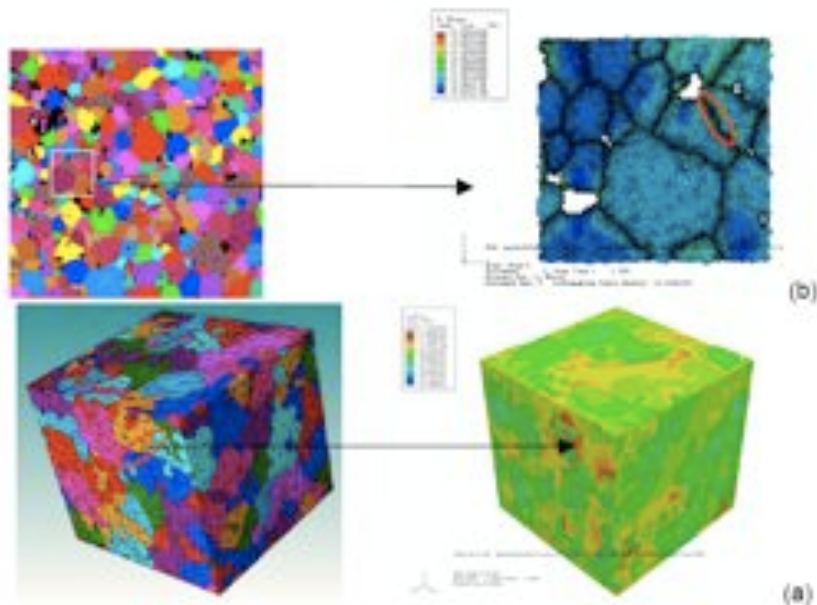
Fig. 27: Von Misses Stresses for (a) 2D and (b) 3D model for uniaxial stress.

Additional nano-indentation characterization was performed on sintered ZrN in the effort to establish and quantify variations in plasticity and elastic modulus based on variations of crystal orientation of individual grains. This study was made on a pellet sintered at 1600 °C. Fiducial marks were created around individual grains to facilitate locating them, as described previously. Nano-indentation, imaging via AFM and SEM; and establishing crystallographic orientation using EBSD were performed on the pellet sample. Seven grains were selected based on their orientation and position on the stereographic triangle, as shown in Fig. 28.
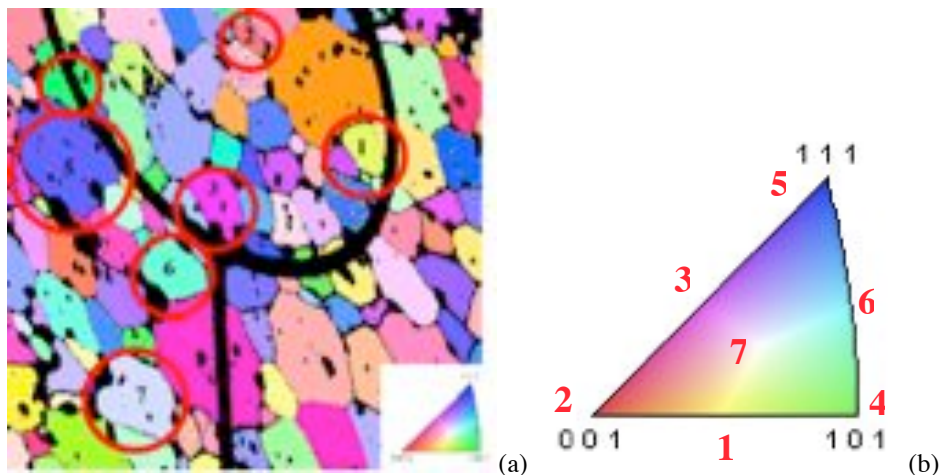
Fig. 28: (a) 1600°C ZrN IPF map with selected grains, (b) stereographic triangle indicating selected grain orientations

Each of the 7 grains was loaded to 5000 μN using a diamond Berkovich nano-indenter. The Reduced Modulus (E_r) of grain 1 was found to be

~220 GPa and the E_r for grain 5 was found to be ~360 GPa. These two grains were selected because they are typically associated with the extreme of the equivalent Young's Modulus for cubic materials. As is typical for cubic materials, the <111> direction was the stiffest. Grain 5, which is located near the 111 direction as determined via EBSD, was clearly the stiffest of the 7 grains tested. This value is very close to the 'accepted' value of E for this material (370-400 GPa). The <001> direction is typically the most compliant in cubic materials, and grain 1, located near the 001 direction, had the lowest stiffness of the grains tested. It should be noted that no displacement jumps were observed during this test.

Correlations of 3D characterization with existing 2D models and experimental results obtained at LANL were made. There was good correlation among experimental measured pellet density and 2D as well as 3D estimations of porosity. Experimental results showed that for a particular ZrN pellet treated at 1600°C, the theoretical density was 93%, which is very similar to the 94% pellet density obtained from the 3D reconstruction model. The distribution of pore size was also examined, and, the distribution that pores followed for 2-D and 3-D data could be seen as a lognormal distribution, as seen in Fig. 29. Two-dimensional images of the microstructure cannot capture the actual size and distribution of the pores, no matter how many images at different regions are analyzed. The 3D model showed a more accurate representation of the pore size and distribution of large pores in the sample.
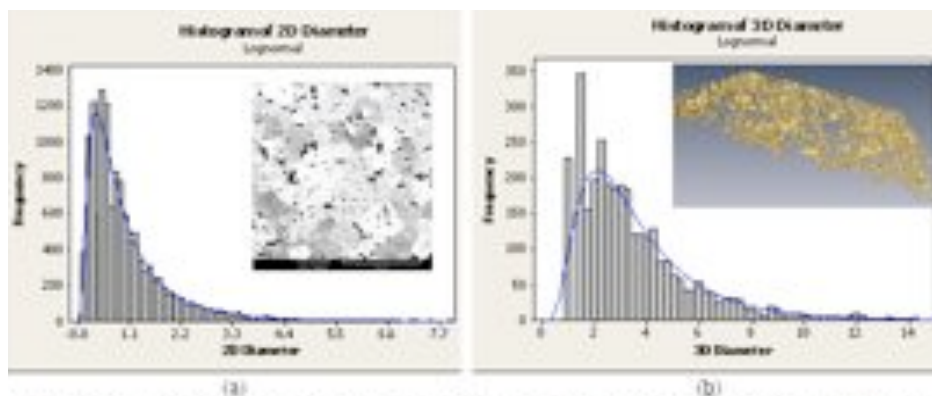
Fig. 29: Histogram of pore diameter distribution for sample sintered at 1600°C in Ar atmosphere (a) 2D data (b) 3D data.

A heat treatment study was performed on sintered ZrN samples that were sintered at three different temperatures (1300°C, 1475°C and 1600°C) in a gettered UHP Argon environment. The heat treatment was conducted for 10 hours at 2000°C in order to simulate the microstructural effects of accidental pellet overheating during service. Each of the 3 pellets tested exhibited distinct microstructural differences before the heat treatment, as previously reported. The microstructure of each of the samples after heat treatment was virtually indiscernible. A "before and after" comparison is

shown in Fig. 30. The fact that the microstructure of all samples was similar despite their initial differences suggests that during the heat treatment the microstructure reached a stable configuration.

(a)   (b)
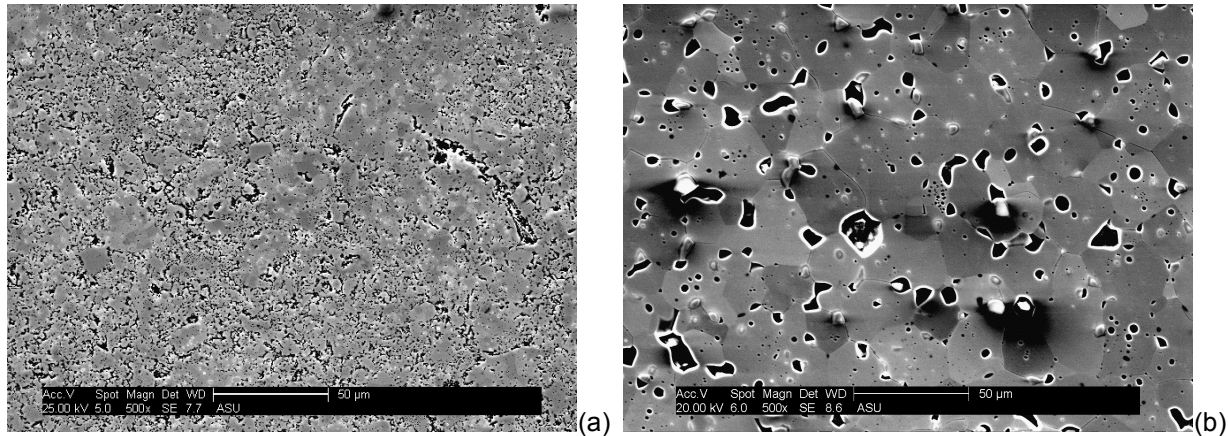
Fig. 30: *Microstructure of ZrN pellets sintered at 1375°C (a) before and (b) after 5-hour heat treatment at 2000°C. Scale Bar = 50μm*

Regarding mechanical behavior of this material, it was previously reported that nano-indentation presented displacement jumps in the load-penetration curves from well-polished monolithic ZrN samples, but these jumps did not appear during nano-indentation of individual grains in sintered ZrN pellets. One possible explanation for the difference in behavior is that the Focused Ion Beam (FIB) used to produce fiducial marks on the surface of the sample before nano-indentation was modifying the surface, either by implantation of Gallium from the ion source of by re-deposition of sputtered ZrN on the polished surface. Additional nano-indentation testing was performed on a sintered ZrN sample without being exposed to FIB milling and clear displacement jumps were observed at loads lower that those that produced jumps in the monolithic samples. The reduction in load may be related to the presence of point defects induced by nitrogen deficiency in the sintered samples, as a consequence of sintering in an Ar atmosphere, or due to the presence of sub-micron porosity.

Goal: Develop Two-Dimensional Finite Element Model that accounts for actual Microstructure
Work towards achievement of goal: The modeling effort work led to the definition of a microstructurally explicit model of the material. In this regard, selection of the region of interest in the pellet is important because it defines the section of the microstructure to be analyzed via the RVE. The idea was to obtain the smallest area on which the grain size distribution had the same basic statistical parameters (average, standard deviation) than those obtained in larger areas. This should result in a large enough RVE to encompass all relevant phenomena to the fuel simulation (elastic, inelastic, thermal and nuclear behavior). First, the homogeneity of the grain distribution as a function of position on the pellet

21

cross-section was checked, as shown in Fig. 31. The results showed that grain size distribution was indeed homogeneous. Then, the grain size distribution for a given location was studied as function of the area characterized, as shown in Fig. 32.
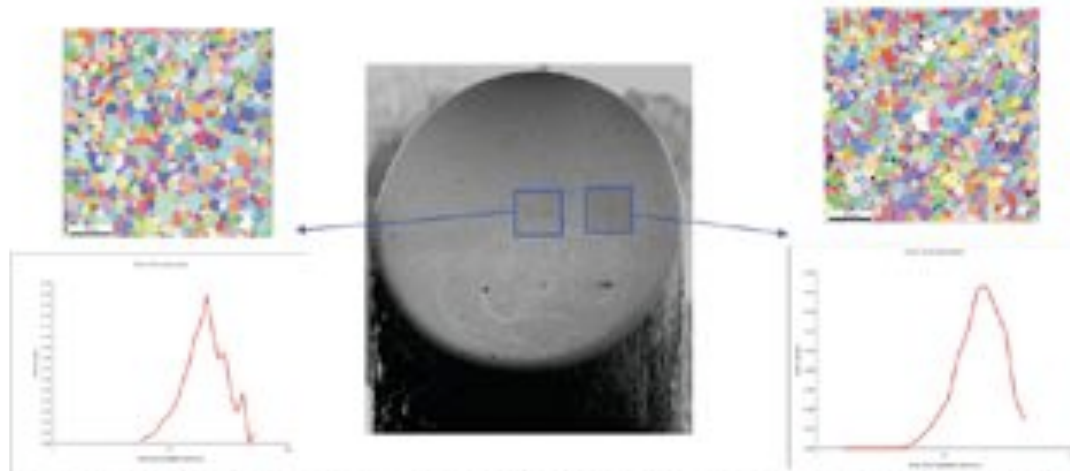
Fig. 31: *EBSD scans and Grain Size Distribution of two different sections in the longitudinal plane of a ZrN pellet sintered at 1600°C.*
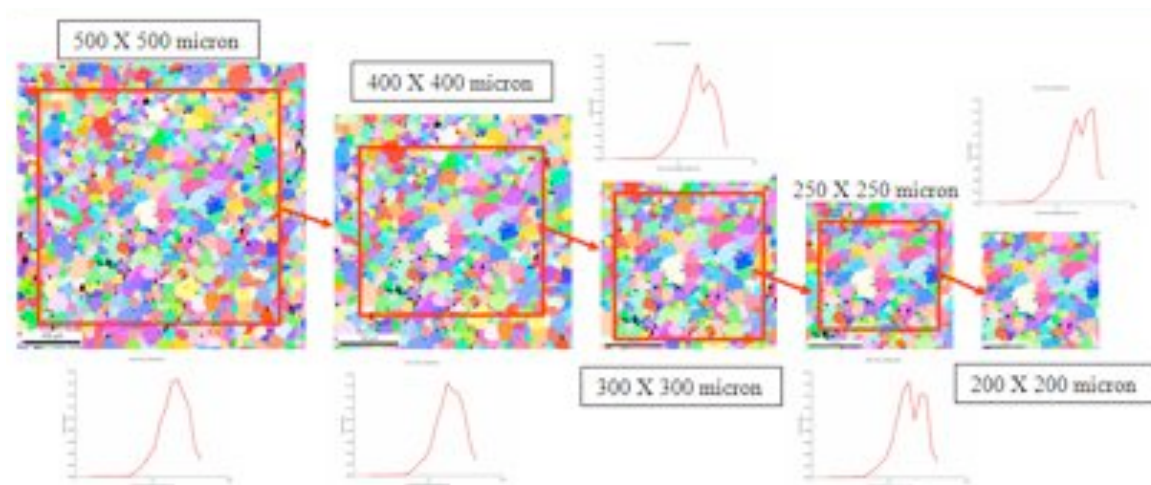
Fig. 32: *RVE size determination from grain size distribution study.*

Mean and standard deviation values were calculated for the different scan areas shown in Fig. 32 and it was found that these two basic values remain fairly constant down to a 250 µm x 250 µm area, which was chosen as the RVE size. The somewhat bimodal distribution shown in Fig. 32 is not accounted for using the mean and standard deviation as parameters, but this likely to be a higher order effect that could be studied in the future.

Literature reviews were conducted to obtain creep and swelling equations for nitride fuels to be applied to the 2D models. In the interim, assumptions made in the AAA Fuels Handbook were used to obtain appropriate equations. In this sense, the scarcity of data for ZrN, PuN

and (Pu,Zr)N creep led to the assumption that the creep rate for fully dense (Pu,Zr)N can be taken to be that of UN. In addition, in the AAA Fuel Handbook, the swelling behavior of (Pu,Zr)N is assumed similar to that to (U,Pu)C.

ABAQUS was used to perform thermo-mechanical simulations, using its built-in capabilities to account for thermal expansion, anisotropic creep and anisotropic radiation swelling/shrinking. The effect of elastic anisotropy was taken into account, by feeding the appropriate anisotropic constants to each grain in the finite element mesh, based on orientations measured from ZrN pellets. Standalone irradiation swelling was run in the 2-D cylindrical FEM with volumetric heat generation as the loading condition (this causes thermal expansion) to see the combined effect of swelling and thermal expansion on the fuel by writing a user sub-routine in ABAQUS twith equations that account for the swelling rates due to solid fission gas products and due to fission gasses. Figure 33 illustrates the radial displacement evolution of the fuel with time for a constant burnup of 1% ran over a period of one month. The temperature boundary condition of the fuel was 600°C.

1 day   15 days   30 days

Fig. 33: *Displacement Evolution of Cylindrical FEM for standalone Swelling simulation.*

Standalone creep was also run with volumetric heat generation as the loading condition by writing a user sub-routine in ABAQUS that contained equations that account for both thermal and irradiation creep rate effects, and its corresponding porosity correction. Figure 34 illustrates the von Misses stress evolution of the fuel with time for a constant burnup of 1% ran over a period of one month. The temperature boundary condition of the fuel is 600°C. The decrease 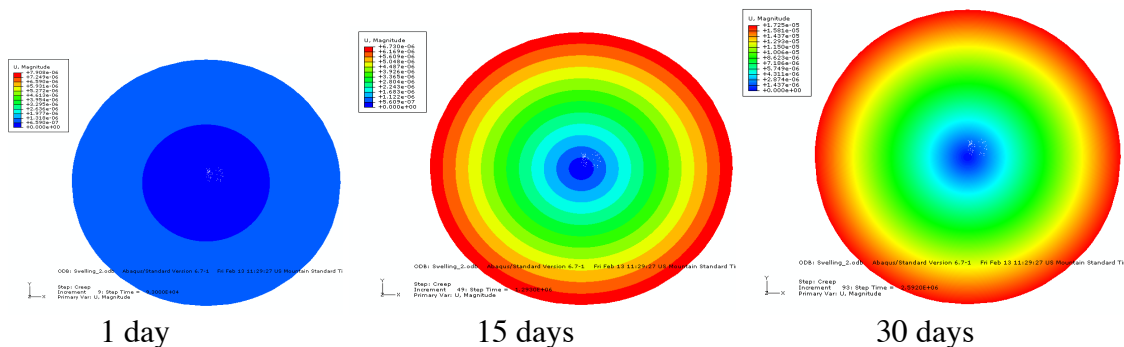on the stress with time is fairly evident, as expected due to the effect of creep. In addition, the results from Fig. 34 show that significant heterogeneity in the stress distribution can exist in the microstructure due to elastic anisotropy alone.

1Day

10 Days

20 Days

30 Days
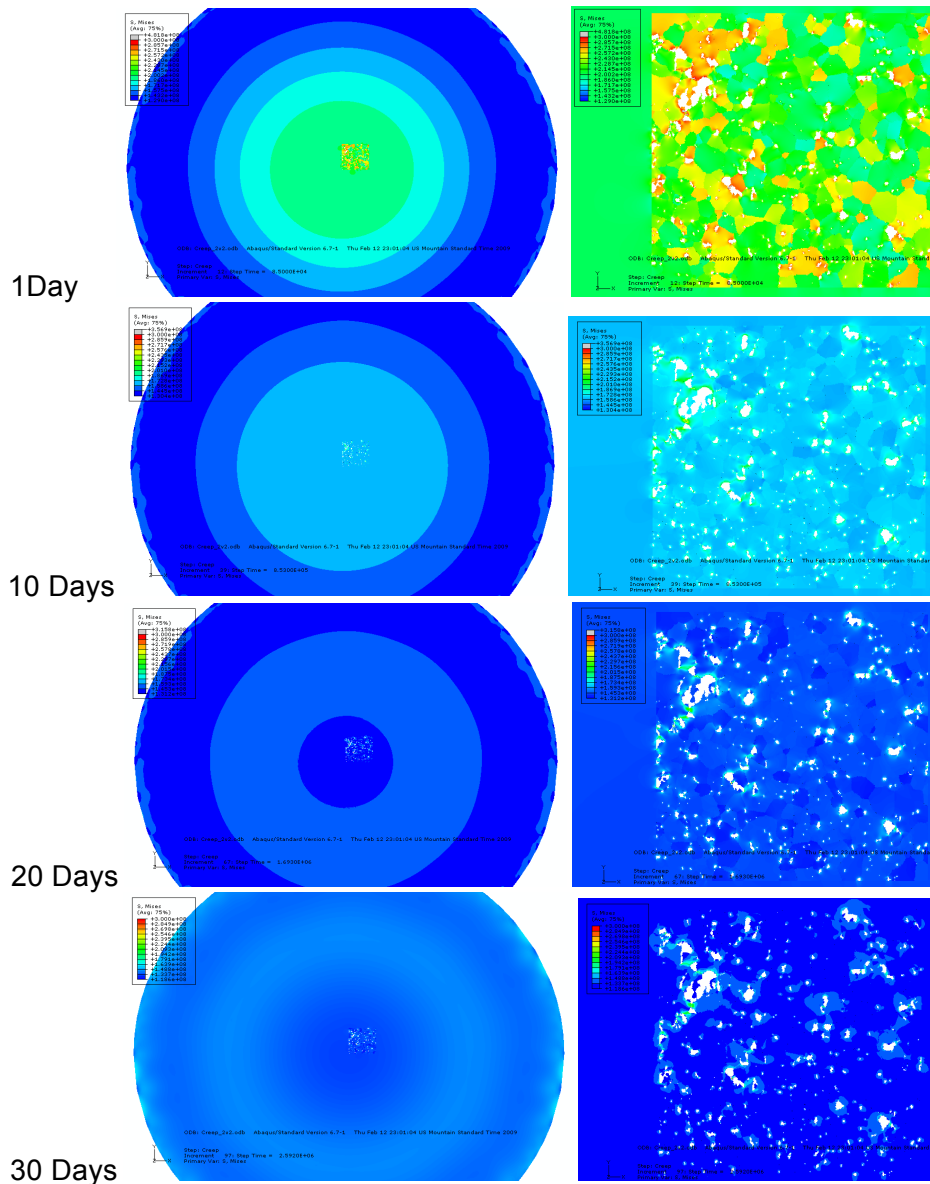
***Fig. 34:** von Misses stress evolution on Cylindrical FEM and RVE for standalone Creep simulation.*

Finally, 3D representations of the microstructure were sought to create 3D fuel simulations. The need for stereology comes to mind, in order to evaluate 3-D characteristics from 2-D sections, which is required when one wants to create artificial 3-D models that reflect a given microstructure. A grain growth code based on simulated annealing was used to generate 3D models with grains. To realize the full potential of the artificial microstructure obtained with the program, the code needs to be modified to obtain the grain size distributions and a technique is required to generate and embed porosity in the artificial RVE. Once the 3-D RVE's are generated, it is possible to then run similar simulations to those done on 2-D models and a clear comparison can be drawn. Figure 35 shows a proof of principle of a 3-D microstructure generated.
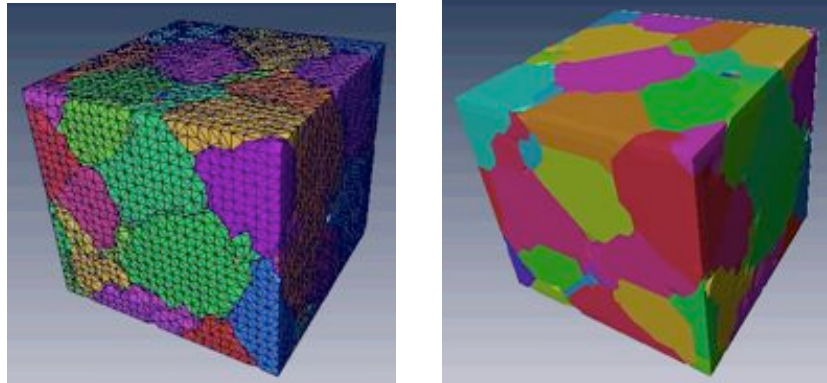
Fig. 35: *Artificial 3-D mesh and microstructure*

Mechanical properties at elevated temperatures were also studied thanks to modifications that were performed on an environmental chamber used for compression testing. The chamber and loading rods were adequate for intermediate temperature (800°C) testing, but they proved to be ill equipped to handle high temperatures (1200°C) and loads in excess of 7kN. Molybdenum heat shields and TZM (metallic alloy containing Tungsten, Zirconium, and Molybdenum) loading rods were added to 'reduce' the system compliance induced by high temperature and retard degradation of the testing equipment.

In previous tests it was found that ZrN pellets would dent stainless steel loading rods, especially at intermediate temperatures (800°C) so SiC disks were used to help distribute the load to the loading rods. This proved to work very well without damaging the SiC disks at 800 °C. ZrN pellets sintered at both 1475°C and 1600°C were tested at 1200°C using a SiC loading surface. Unfortunately, both samples proved to be 'less-ductile' than SiC and significantly deformed the SiC loading disks. Samples sintered at 1475°C did not break in compression before the test reached its displacement limit with a loading of nearly 7000 N, which is nearly the failure point of similar samples when tested at 800 °C. It was very clear that the SiC deformed significantly, but it is unclear if plasticity occurred in the ZrN sample as well. Samples sintered at 1600 °C did reach failure using a SiC loading surface (~5500 N), but significant SiC deformation was produced in that case also. In order to reduce this effect, TZM disks were used because it was observed that the TZM loading rod was also able to deform the SiC loading disks. The TZM loading disks were found to be much stiffer than the SiC disks at 1200 °C, but unfortunately both ZrN samples were still able to deform the loading surface. This unfortunately affects the reliability of the loading curves. However, it is known that the critical loading of the 1475°C sintered samples was similar in both 800 °C and 1200 °C tests and increased for samples sintered at 1600 °C when tested at 800 °C and 1200 °C. In addition, initial characterization indicated a significant difference in the

fracture characteristics of the two sample types tested at 1200 °C compared to the results found in 800 °C tests, as shown in Fig. 36.

(a)
(b)
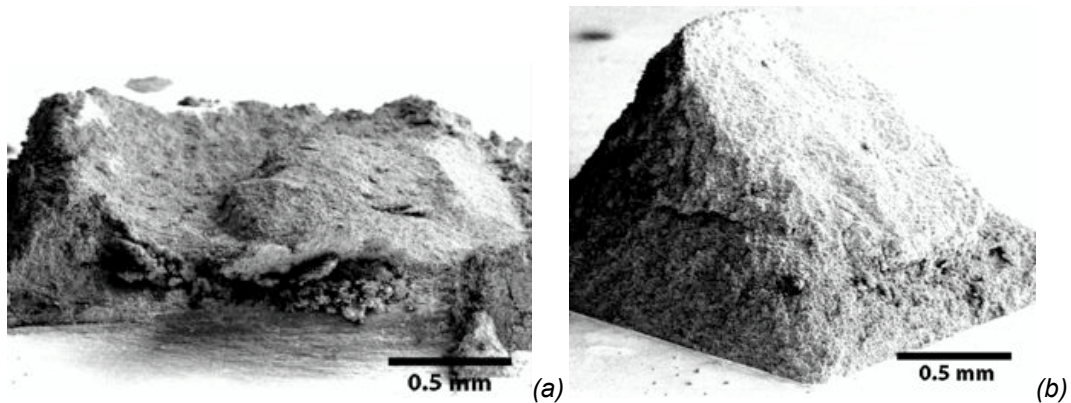
Fig. 36: *Differences in fracture behavior of 1200°C compression tests of samples sintered at (a) 1475°C, 0.5 mm scale bar (b) 1600°C, 0.5 mm scale bar.*

While the fracture behavior of 1475°C samples (Fig. 36a) tested at 1200 °C is consistent with the results found in 800 °C compression tests, the fracture behavior of 1600 °C samples (Fig. 36b) tested at 1200 °C is quite different from the results found in 800 °C tests. The 1600 °C samples produced a 'pyramid' shape when tested at 1200 °C, which has a striking resemblance to the behavior found during compression tests of semi-ductile materials. It is possible that a ductile-brittle transition temperature exists for ZrN and it may be near 1200 °C. The fracture surface of the 1600 °C sample exhibited two regions that had very different microstructural characteristics as shown in Fig. 37.

(a)
(b)
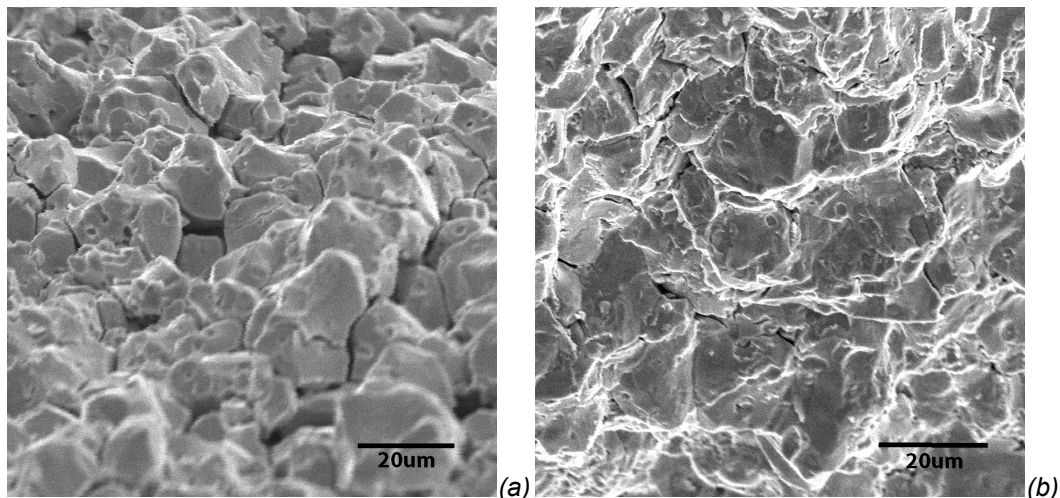
Fig. 37: *Fracture surfaces of a 1600 °C sample tested at 1200 °C. (a) Brittle region, 20μm scale bar (b) ductile region, 20μm scale bar*

It was found that the upper face of the fracture surface (one of the inclined surfaces of the pyramid) consists of a region that is microstructurally consistent with ductile rupture/tearing and the side faces have a fracture surface that is consistent with the brittle intergranular failure previously found in intermediate temperature (800 °C) testing results.

Another important aspect of this project was to extend the techniques developed to material closer to actual fuels, particularly those containing depleted uranium. The design and fabrication of a glovebox to store and handle depleted uranium samples were completed under this project. The construction involved building a transfer chamber, which was built to be airtight and easy to operate and the doors have counterweights to assist motion and a sliding drawer to further assist the operator. O-ring seals along with cam levers are in place to keep the glovebox sealed. In addition, a panel was built to house the valves and nuclear filter elements in an orderly fashion. Some of the parts that were purchased for this facility include locks, nuclear filters, a vacuum pump, and a wand-style Geiger counter. The locks have been fitted to the doors to prevent unauthorized access. The nuclear filter is designed to catch all particles and is used inline with the flow created by the vacuum pump that evacuates that airlock of the transfer chamber. The Geiger counter is highly accurate and usable in and out of the glovebox.

The glovebox, along with a depleted Uranium Oxide sample provided by collaborators at Los Alamos National Laboratory, was used to hold and handle the sample, the microstructure of which was characterized using regular SEM and EBSD, as shown in Fig. 38.
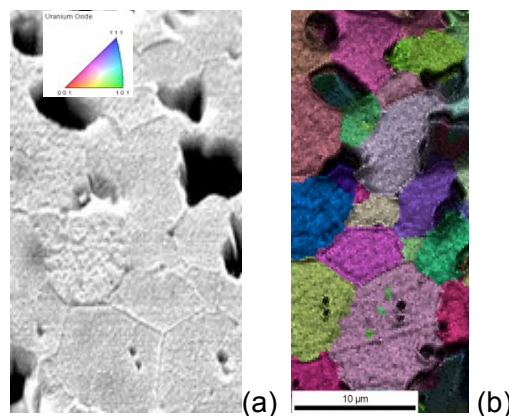

Fig. 38. (a) SEM image of the microstructure of a depleted-UO_2 pellet (b) EBSD map showing grain crystallography and porosity.

Patents: N/A

Publications/Presentations:

Fourteen quarterly reports were submitted to LANL on activities related to investigations of mechanical behavior and microstructural characterization on monolithic ZrN, sintered ZrN, YSZ processed using conventional sintering and microwaves, as well as information on characterization of depleted uranium oxide. In addition, a manuscript on surface plasticity on ZrN is in the final stages of completion.

Journal articles include:

I. Han, P. Peralta, K. J. McClellan and K. Wheeler, "Microstructural Evolution and Grain Morphology Studies in ZrN." TMS Letters, 2(3), 2005, 75.

K. Wheeler, P. Peralta, M. Parra, K. J. McClellan, J. Dunwoody, G. Egeland, *"Effect of Sintering Conditions on the Microstructure and Mechanical Properties of ZrN as a surrogate for Actinide Nitride Fuels"*, Journal of Nuclear Materials, vol. 366, 306-316, 2007 (copy attached).

R. R. Thridandapani, C. E. Folger, D. C. Folz, D.E. Clark, K. Wheeler, P. Peralta, "Microwave sintering of 8 mol% yttria-zirconia (8YZ): An inert matrix material for nuclear fuel applications", Journal of Nuclear Materials, vol. 384, 153-157, 2009 (copy attached).

Conference proceedings include

D. D. Byler, K. J. McClellan, J. A. Valdez, P. D. Peralta and K. Wheeler, "Investigation of Aluminides as Potential Matrix Materials for Inert Matrix Nuclear Fuels." Ceramic Engineering and Science Proceedings, 27(5), pp. 89-99, (2006).
J. T. Dunwoody, C. R. Stanek, K. J. McClellan, S. L.Voit, T. Hartmann, K. Wheeler, M. Parra, and P. D. Peralta, "Optimization of Sintering Parameters for Nitride Transmutation Fuels." Ceramic Engineering and Science Proceedings, **27**(5), pp. 29-38, (2006).
K. Wheeler, P. Peralta, K. McClellan, "Variations in Plasticity and Fracture with Respect to Crystallographic Orientation in Individual Grains of Sintered ZrN Pellets," TMS Supplemental Proceedings Volume 3: General Paper Selections (2008).
K. Wheeler, P. Peralta, K. McClellan, "Multi-Temperature Uniaxial Compression Testing of Sintered ZrN and (Zr,Ti)N Pellets as Surrogates for PuN and (Pu,Zr)N Fuels." TMS Supplemental Proceedings Volume 3: General Paper Selections (2008).
M. Parra, S. Park, K. Wheeler, P. Peralta, K. McClellan, "Porosity Distribution and Effective Elastic Modulus in ZrN as a Surrogate for PuN: Comparisons Between 2-D and 3-D Measurements and Models," TMS Supplemental Proceedings Volume 3: General Paper Selections (2008).
M. Parra, S. Park, K. Wheeler, P. Peralta, K. McClellan, "Evaluation of Variability on the Thermomechanical Response of Nitride Nuclear Fuels

through Microstructurally Explicit Models," TMS Supplemental
Proceedings Volume 3: General Paper Selections (2008).

Conference Presentations

K. Wheeler, M. Parra, J. Dunwoody, P. Peralta and K. J. McClellan,
"Mechanical Properties and Microstructure of ZrN Pellets as Surrogates
for Nitride Fuels: Effect of Sintering Conditions." TMS Annual Meeting
San Antonio, TX, 2006.
K. Wheeler, P. Peralta, M. Parra-Garcia and K. J. McCllelan, "Mechanical
Properties and Microstructure of (Zr, Ti)N Pellets as Surrogates for
(Pu,Zr)N Fuel Pellets." TMS Annual Meeting, Orlando, FL, 2007.
M. Parra-Garcia, A. Batwal, and P. Peralta, "Effects of Microstructural
Heterogeneity on Stress Variability in ZrN Pellets." TMS Annual Meeting,
Orlando, FL, 2007.
K. Wheeler, P. Peralta, K. McClellan, "Variations in Plasticity and Fracture
with Respect to Crystallographic Orientation in Individual Grains of
Sintered ZrN Pellets." TMS Annual Meeting, New Orleans, LA, 2008.
K. Wheeler, P. Peralta, K. McClellan, "Multi-Temperature Uniaxial
Compression Testing of Sintered ZrN and (Zr,Ti)N Pellets as Surrogates
for PuN and (Pu,Zr)N Fuels." TMS Annual Meeting, New Orleans, LA,
2008.
M. Parra, S. Park, K. Wheeler, P. Peralta, K. McClellan, "Porosity
Distribution and Effective Elastic Modulus in ZrN as a Surrogate for PuN:
Comparisons Between 2-D and 3-D Measurements and Models." TMS
Annual Meeting, New Orleans, LA, 2008.
M. Parra, S. Park, K. Wheeler, P. Peralta, K. McClellan, "Evaluation of
Variability on the Thermomechanical Response of Nitride Nuclear Fuels
through Microstructurally Explicit Models." TMS Annual Meeting, New
Orleans, LA, 2008.
M. Parra Garcia, K. Wheeler, K. McClellan and P. Peralta, "Quantification
of Microstructurally Induced Variability on the Thermo-Mechanical
Response of Nitride Nuclear Fuels through Finite Element Models." TMS
Annual Meeting, San Francisco, CA, 2009.
K.Wheeler, P. Peralta, K. J. McClellan, "Microstructural Evolution and
Multi-Scale Characterization of Sintered ZrN as a Surrogate for PuN Fuel
Pellets." TMS Annual Meeting, San Francisco, CA, 2009.

Milestone Status Table:

ID Number	Task / Milestone Description	Planned Completion	Actual Completion	Comments
1	Development of Processing and Characterization of Surrogate Fuel Pellets			
1.1	Establish Surrogates for PuN and Attempt Fabrication of Surrogate Pellets	3/15/06	3/01/06	
1.2	Microstructural Characterization of Pellets Produced by Parametric Sintering Study	9/15/05	11/15/05	
1.3	Processing Optimization and Establishment of Microstructural Evolution	12/15/05	12/15/05	
1.4	Measurement of Mechanical Properties at Room Temperature	3/15/06	12/15/05	
2	Characterization of Mechanical Properties at Intermediate Temperatures and Microstructural Evolution of Pellets			
2.1	Apply Processing from Surrogates to Actual Fuels.	6/15/06	N/A	
2.2	Characterize Mechanical Properties of Surrogates at Intermediate Temperatures	9/15/06	12/15/06	
2.3	Characterize Pellets Tested at Intermediate Temperatures	12/15/06	2/15/07	
2.4	Correlate Mechanical Properties and Microstructure of Surrogate Pellets	12/1/08	12/1/08	
3	Establish Mechanical Behavior and Microstructural Evolution of Surrogate Pellets at High Temperatures			
3.1	Creep Testing and Recrystallization Studies	6/15/08	11/1/08	
3.2	Analysis of High Temperature Deformation Mechanisms	12/1/08	12/15/08	
3.3	Formulate Models for Deformation Mechanisms	12/15/08	12/15/08	
3.4	Two-Dimensional Finite Element Model Accounting for Actual Microstructure	12/15/08	12/1/08	
3.5	Final Report	1/1/09	3/1/09	

Budget Data: 3/14/05-12/15/08

Phase / Budget Period			Approved Spending Plan			Actual Spent to Date		
			DOE Amount	Cost Share	Total	DOE Amount	Cost Share	Total
	From	To						
Year 1	3/14/05	3/13/06	150,267	0	150,267	143,021	0	143,021
Year 2	3/14/06	3/13/07	150,263	0	150,263	96,331	0	96,331
Year 3	3/14/07	3/13/08	150,176	0	150,176	130,013	0	130,013
Year 4	3/14/08	12/1/08				62,298		62,298
Year 5								
		Totals	450,706	0	450,706	431,663	0	431,663

ELSEVIER

Effect of sintering conditions on the microstructure and mechanical properties of ZrN as a surrogate for actinide nitride fuels

K. Wheeler [a,b,*], P. Peralta [a], M. Parra [a], K. McClellan [b], J. Dunwoody [c], G. Egeland [b]

[a] *Mechanical and Aerospace Engineering, Arizona State University, P.O. Box 876106, Tempe, AZ 85287, USA*
[b] *Material Science and Technology Division, Los Alamos National Laboratory, Los Alamos, NM 87545, USA*
[c] *Nuclear Materials Technology Division, Los Alamos National Laboratory, Los Alamos, NM 87545, USA*

Abstract

Pellets of sintered ZrN were studied to optimize the mechanical properties and microstructures needed in nitride fuel pellets, using ZrN as a surrogate for actinide nitrides and as potential component in low fertile and inert matrix fuels. Samples were prepared via sintering in either Ar or N_2 (with and without 6% H_2) and at 1300 °C or 1600 °C. A significant difference in the hardness was measured ranging from 1000 (Kg/mm^2) in samples sintered at 1600 °C in argon to 100 (Kg/mm^2) in samples sintered at 1300 °C in nitrogen. Samples with 6% hydrogen added to the sintering environment experienced a decrease in hardness, as well as an increase in intergranular cracking as compared to samples sintered without hydrogen, suggesting hydrogen embrittlement. Grain size was more uniform in samples sintered in pure Ar as compared to Ar–H_2, while the latter had a larger fraction of high angle grain boundaries than the former. Cracking around indents had a clear tendency to follow high angle boundaries, which were found to be intrinsically weak in ZrN.
Published by Elsevier B.V.

PACS: 81.05.Je; 89.30.Gg; 62.20.Qp; 81.20.Ev

1. Introduction

Nuclear fuels based on actinide nitrides, particularly uranium and plutonium mononitrides and their solid solutions, have considerable potential

for advanced applications, including nuclear power sources and nuclear–thermal propulsion for space vehicles [1–4]. Research carried out so far indicates that nitride fuels have a series of quite desirable properties, including high thermal conductivity, high melting point, high actinide atomic density, low swelling and low fission gas release, among others [2,3,5]. Interest on nitride based fuels for advanced applications has arisen within the advanced fuel cycle initiative (AFCI) of the US Department of Energy (DOE), since these materials

are potential candidates for the development of fuels that could potentially enhance proliferation resistance of next generation of nuclear reactors, and for waste reduction via transmutation of transuranic fission products [6], thus reducing the environmental impact of nuclear energy production by reducing the long-lived radiation sources by a factor of 10 and radiotoxicity by a factor of 100 [1].

Due to the high cost associated with the development, testing and characterization of transuranic fuels, ZrN has been proposed as a surrogate material based on the fact that it is isostructural with many actinide mononitrides (NaCl structure), its ability to form a solid solution with PuN [7], the similarities observed between its microstructure and that of actinide nitrides [7], as well as being a possible inert matrix material to host minor actinide (MA: Np, Am, Cm) materials during transmutation [8–11].

The addition of the transuranics complicates the structural requirements of sintered fuel pellets for a few reasons. The fact that Am has a tendency to vaporize under typical sintering conditions [12,13] has called for the development of alternative sintering parameters to reduce Am losses. Furthermore, [241]Am can produce a large quantity of helium during irradiation from α-decay [14]. This extra gas could increase pellet swelling [15], cracking and accelerate the degradation of the mechanical integrity of the fuel. One possible approach for the controlled release of this extra gas requires the fuel pellet to have an increased percentage of open porosity while maintaining a high level of hardness and fracture toughness.

In order to optimize the mechanical properties and porosity distributions needed in sintered nitride fuel pellets, test samples of ZrN were prepared using a variety of sintering conditions. Relationships between the resulting microstructure, processing and mechanical properties were established and correlated with potential fuel performance. These correlations, along with the methodologies used, which include modern methodologies such as OIM that have not been extensively used to characterize nuclear fuels, can be useful in the development of nitride fuels for space reactors and other advanced applications.

2. Experimental procedure

The sintered ZrN pellets used for this study were prepared at Los Alamos National Laboratory (LANL) under various atmospheres and sintering temperatures. All of the pellets were made from the same batch of commercial –325 mesh ZrN powder, mixed with a lube and binder (0.2 wt% Zn Stearate and 0.3 wt% PEG) in a nitrogen gas filled glove box with <10 ppm O_2. Batches of 5 g of this mixture were milled in a Spex mill for 45 min and then pressed at 250 MPa. These pellets were then sintered at either 1600 °C or 1300 °C for 10 h plus thermal ramp time. Four different atmospheres were used for this study, UHP–Ar, Ar–6% H_2, UHP–N_2 and N_2–6% H_2. Pure ZrN powder was also poured over the pressed green pellets so that the powder could act as a sacrificial oxidation target thus reducing oxygen contamination. Note that the study performed by Matthews et al. [3] on UN for space fuels used sintering to produce fuel pellets, but only under pure gettered Ar, so a comparison can be established with the other sintering environments used here.

Metallographic samples were taken from the pellet's radial plane and polished using a 6 μm diamond impregnated disk, SiC paper (600, 800, and 1200 grit) and then finished with 0.05 μm colloidal silica. These metallographic samples were also used to measure Vickers hardness using a load of 500 g, which was found to be large enough to average out microstructural variations such as porosity and grain formations.

Fifteen indents per sample were made and optical microscopy was used to measure their diagonals for hardness calculation.

A small portion of the sintered samples were ground in an agate mortar along with high purity Si to perform standard X-ray powder diffraction using a Rigaku D/Max-IIB diffractometer with Cu Kα radiation. Intensity data were taken every 0.02° scanning at a rate of 2°/min. The Si served as an internal reference to correct for possible angular misalignments. The resulting diffraction patterns were indexed using standard databases and commercial software. Lattice parameters were determined by using a least squares fitting of the ZrN peaks assuming a NaCl structure.

The microstructure of the samples was characterized using scanning electron microscopy (SEM) and orientation imaging microscopy (OIM). SEM was performed in an FEI XL-30 environmental scanning electron microscope operating at 20 kV. Additional SEM and OIM imaging were performed on a Camscan scanning electron microscope with an EDAX/TSL OIM system.

A pellet of ZrN was prepared via Hot Isostatic Pressing (HIP) and was heat-treated for 36 h at 1400 °C in an N_2–6% H_2 environment. The sample was covered in pure ZrN powder during this heat treatment to reduce sample oxidation. Transmission Electron Microscopy (TEM) was performed on sections of this sample, before and after heat-treatment using a Philips/FEI CM-30 using a 300 keV beam.

3. Results and discussion

3.1. Physical characteristics

The sintered density and the open and closed porosities of the samples are shown in Fig. 1. It can be seen that the sintered density of the material is a strong function of temperature and sintering gas (Ar or N_2), but it does not depend strongly on the presence of hydrogen in the gas stream, and there is just a slight trend for lower density in the presence of hydrogen. The effect of sintering gas is quite significant, since it is clear from Fig. 1(a) that the density of samples sintered in Ar are much higher than that of samples sintered in N_2 at the same temperature. In fact, sintering at 1300 °C in Ar is roughly equivalent to sintering in N at 1600 °C. This indicates that the kinetics of the sintering process is strongly dependent on the sintering atmosphere.

A densification curve was made relating sample density to sintering temperature for each of the four sintering environments used for this study and is shown in Fig. 2. From this curve we can see that the N_2 sintered samples are only in the intermediate stage of the sintering process for the temperatures used for this study [16], while the Ar sintered samples are well into the final stages of sintering and appear to have reached thermal stability. Adding hydrogen to the sintering environment seems to have a retarding effect on the sintering and densification of the test samples as seen by the drop in sample density at a given temperature when compared to the samples that were sintered without hydrogen.

The porosity also changes significantly with temperature and sintering gas, as shown in Fig. 1(b) and (c), where it can been seen in that the samples sintered in a 6% hydrogen environment show an increase in open porosity and a small decrease in closed porosity compared to samples sintered without hydrogen.
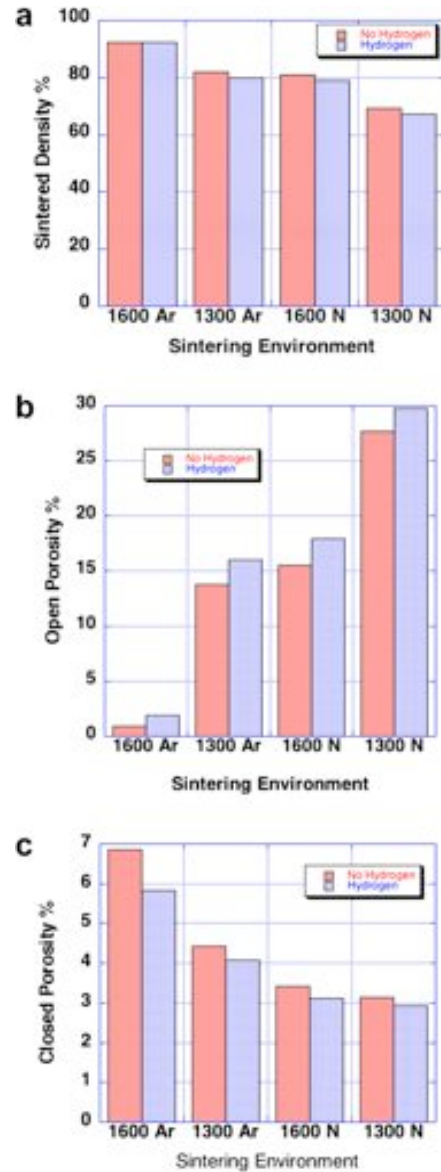

Fig. 1. (a) Sintered density; (b) open and (c) closed porosity as a function of sintering temperature and atmosphere.

3.2. Microstructure

A decrease in closed porosity produced by hydrogen can be noticed in the microstructure of two samples having similar densities, as shown in Figs. 3 and 1(c), where samples sintered with and without hydrogen are compared. Note that the sample sintered in Ar–6% H_2 (Fig. 3(b)) shows a reduction of closed porosity over the sample sintered in pure Ar (Fig. 3(a)). Most of the closed porosity in these samples looks like bubble formations located on
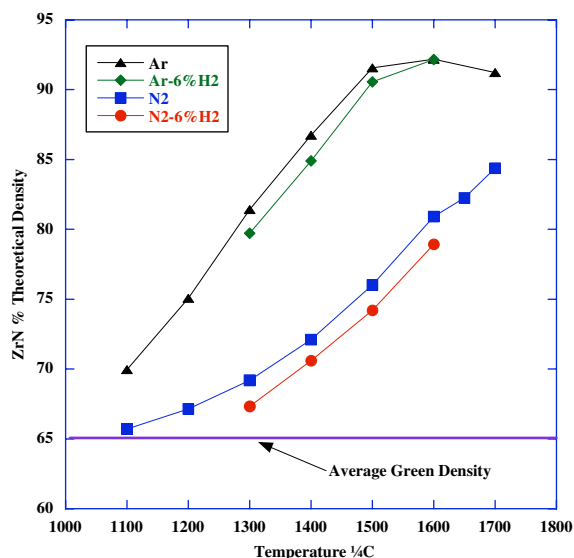
Fig. 2. Densification behavior of ZrN pellets sintered under various atmospheres.

the interior of a grain, particularly at large densities, as can be seen in the SEM pictures of the resulting microstructures shown in Fig. 4. This assumption is made based on the fact that the most energetically favorable shape of a bubble or void is a sphere [17], rather than an irregular or sharp edged shape or a cylinder. So the circular voids in the two-dimensional cross section can be assumed to have been nearly spherical and therefore closed porosity.

Note from Fig. 5(a) that samples sintered in argon at 1600 °C show large pores with clear and porosity coarsening mechanisms associated with grain boundary sweeping. The circular cross section of the pores in the dense samples sintered at 1600 °C in Ar, along with the well-developed grain structure, adds to the suggestion that the microstructure is reaching thermal stability.

The sample sintered in nitrogen at 1300 °C (Fig. 5(b)), shows signs of grain growth by particle coalescence, which is to be expected in the earlier stages of the sintering process. One of the most noticeable microstructural differences of the samples shown in Fig. 4 is the effect that the sintering atmosphere has on grain evolution. There were no observations of fine particles remaining in samples sintered in argon, while all samples sintered in nitrogen exhibited incomplete sintering to some extent. The microstructure of the nitrogen-sintered samples has two distinct regions: dense clusters of small grains and sparse regions of particles that seem to have very little interconnection (Figs. 4(b) and 5(b)). Possible reasons for this could be due to differences in solubility and chemical activity of the two sintering gasses, as well as the population of point defects they produce [17] during sintering. In this sense, the point defects produced by changes in stoichiometry are known to have large effects on transport kinetics in nuclear fuels [2,3,15]. For example, uranium nitride that is nitrogen deficient has been shown to experience more swelling and gas release by accumulation of fission gases on the grain boundaries than nitrogen rich UN [2]. This is probably an effect of enhanced mobility of fission gas due to point defects produced by deviation from stoichiometry, in a manner similar to that observed in oxygen rich UO_2 [15]. The accelerated sintering kinetics under Ar strongly suggests the presence of point defects enhancing mass transport in ZrN.

The lattice parameters measured in samples sintered under Ar and N_2 offer supporting evidence for a difference in defect population between the two sintering conditions. The resulting lattice parameters are shown in Fig. 6. Note from this figure that the lattice parameters are not affected strongly by the presence of hydrogen in the sintering
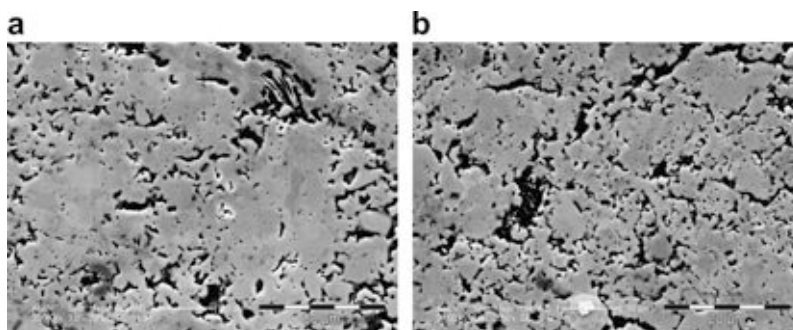

Fig. 3. Typical microstructure of: (a) 1300 °C Ar and (b) 1300 °C Ar–6% H. Scale bar = 20 µm in both figures.
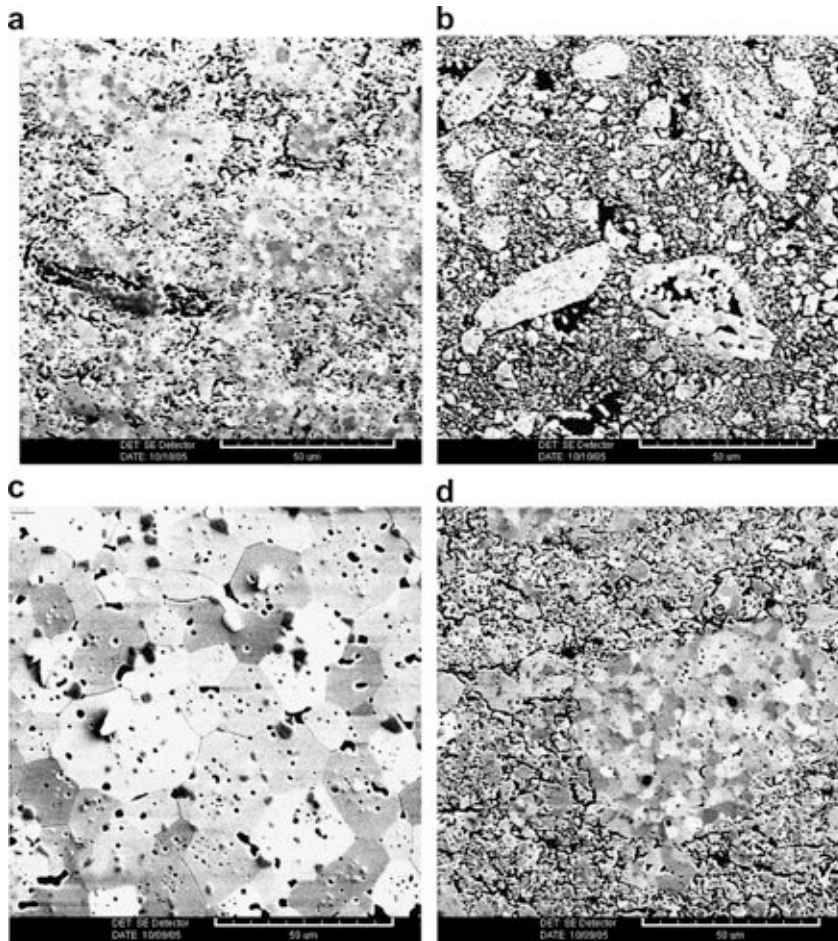
Fig. 4. Typical microstructure of sintered samples. (a) Ar, 1300 °C, (b) N, 1300 °C, (c) Ar, 1600 °C, (d) N, 1600 °C. Scale bar is 50 μm in all images.
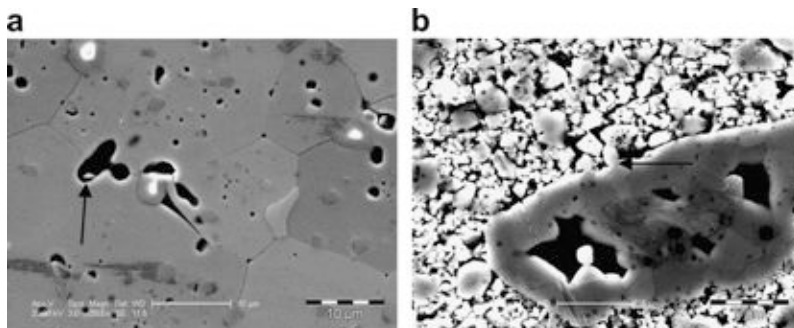
Fig. 5. (a) Pore coalescence (arrow), 1600 °C Argon. Scale bar = 10 μm. (b) Grain growth by particle coalescence (arrow), 1300 °C N. Scale bar = 5 μm.

environment, since the differences are within the error bars shown; however, the differences between Ar and N_2 are significant and larger than the error bars. This result indicates that the sintering atmosphere indeed makes a difference on the material

lattice, probably through the generation of point defects. The trend observed, though, is somewhat hard to explain at this time, since the lattice parameter measured for the Ar sample is somewhat closer to the value of a standard database, 4.578 Å

Fig. 6. Lattice parameter in samples sintered at 1600 °C under different atmospheres.
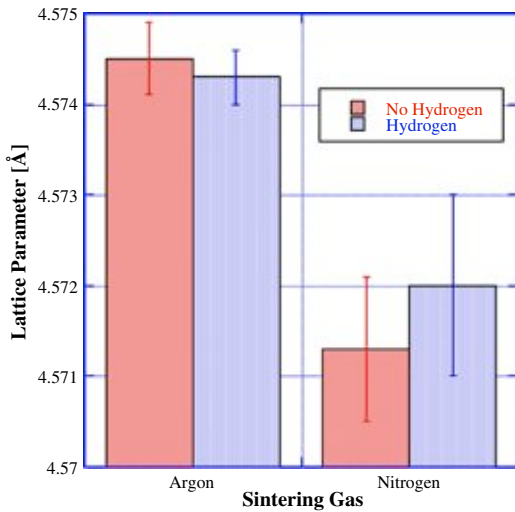
[18], than that of the samples sintered in N_2, which is smaller. The possible reasons for this are being explored. However, the difference between the two cases is clear and measurable, and it points to structural changes induced during sintering, given that the initial powder was the same for both samples.

The difference in microstructure induced by changes in sintering gas were further explored in high density samples, since they present a microstructure that is quite similar to that reported in [3] for UN as a potential material for space fuels. The large grains present in the samples sintered in Ar at high temperature make them suitable to study using orientation imaging microscopy (OIM), as described in the next section.

3.3. Orientation imaging microscopy (OIM)

The orientation data gathered with OIM was used to obtain grain size and grain boundary misorientation distributions for samples sintered in Ar with and without hydrogen, as shown in Fig. 7. The sample size for this study contained ≈1500 grains for each of the two materials. The data were filtered to remove points with more than 10% probability of being incorrect, and the porosity was 'cleaned up' in such a way that only the underlying grain structure was used for the measurement. The differences between the grain size distributions of the samples sintered with and without hydrogen are subtle, but interesting. The average grain size for both of them is about the same at about 20 μm, which is the grain size required for UN in space applications according to [3], pointing to Ar as the best choice for sintering environment in this case, although there is some evidence that vacuum can also be quite effective [2]. Note that the sample sintered in Ar has a sharper maximum, which implies that the grain size is actually more uniform in this sample than in the specimen sintered in Ar–6% H_2, where the distribution is 'blunt' around the maximum value, pointing to a wider distribution of grain sizes. Furthermore, there are two local maxima beyond the average value, which means that there is a tendency for certain grains to grow larger than in the sample sintered in Ar. It should be noted that the variation of the grain size distribution of the Ar–6% H_2 sintered samples could be linked to grain boundary interference by either pores, gas bubbles or solid inclusions based on the tendency for these interactions to create bimodal grain size distributions [16].
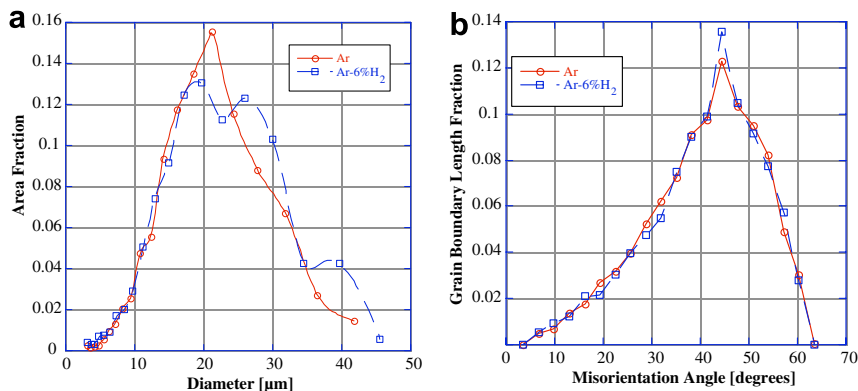

Fig. 7. (a) Grain size distribution and (b) grain boundary misorientation distribution for samples sintered in Ar and Ar–6% H at 1600 °C.

Regarding the distribution of misorientation angles, note that the situation is reversed: the sample sintered in Ar–6% H_2 has a sharper peak than the sample sintered in pure Ar, which means that samples sintered in Ar–6% H_2 have a higher fraction of these boundaries. These peaks are around 45° for both specimens, so that grain boundaries for the two sintering conditions tend to be 'high angle' [19], with a higher fraction of them in samples sintered under the argon–hydrogen atmosphere.

The microstructural differences described above also affected the mechanical response of the samples, which will be discussed below.

3.4. Mechanical response

The Vickers hardness of the samples used in this study is shown in Fig. 8. There is a significant difference between samples sintered in N_2 at 1300 °C and samples sintered in Ar at 1600 °C. In addition, note that the hardness of samples sintered with a 6% addition of hydrogen is lower compared to similar samples sintered without hydrogen. All these trends are likely linked to the differences in microstructure among the samples.

Comparison of the indents made in high density samples sintered with and without hydrogen reveal that indents induced intergranular cracking in both cases, which is not surprising given the presence of a large fraction of high angle boundaries (Fig. 7(b)). However, the region affected by cracking is larger in specimens sintered in Ar–6% H_2, as can be seen in Fig. 9. The fact that the intergranular cracking extends farther in the sample sintered in Ar–6% H_2 suggests that this sample presents relatively weaker grain boundary strength. This agrees with the fact that the average hardness for samples sin-
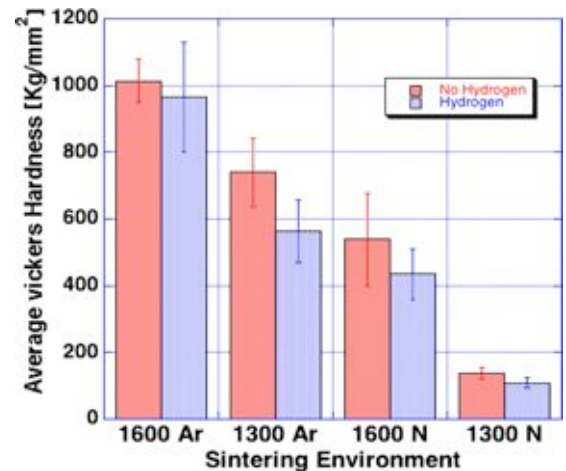

Fig. 8. Vickers hardness as a function of sintering temperature and atmosphere for equivalent load.

tered in Ar–6% H_2 is lower and the scatter larger than for samples sintered in pure Ar. The low hardness of samples sintered in N_2, with and without hydrogen, as compared to the hardness of samples sintered in Ar, is simply a result of the differences in density and microstructure. A lower hardness can indeed be expected due to the higher porosity and reduced grain interconnection due to poor sintering in N_2.

The OIM data was also used to establish correlations between the local crystallographic environment around the indents and the fracture behavior. Figs. 10 and 11 show 'typical' indents in samples sintered in Ar and Ar–6% H_2, respectively, along with inverse pole figure (IPF) maps of the grains around these indents. In these IPF maps, the color of each grain correlates to the crystallographic orientation of its normal (coming out of
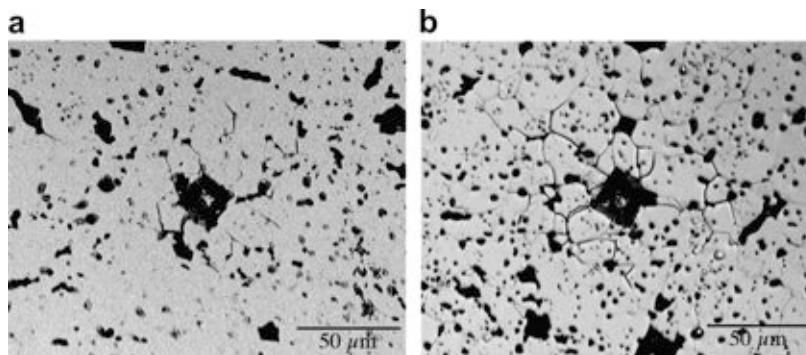

Fig. 9. Optical images of Vickers indents (500 g load) of (a) 1600 °C Ar; (b) 1600 °C Ar–6% H_2 samples. The scale bar in both figures is 50 μm long.
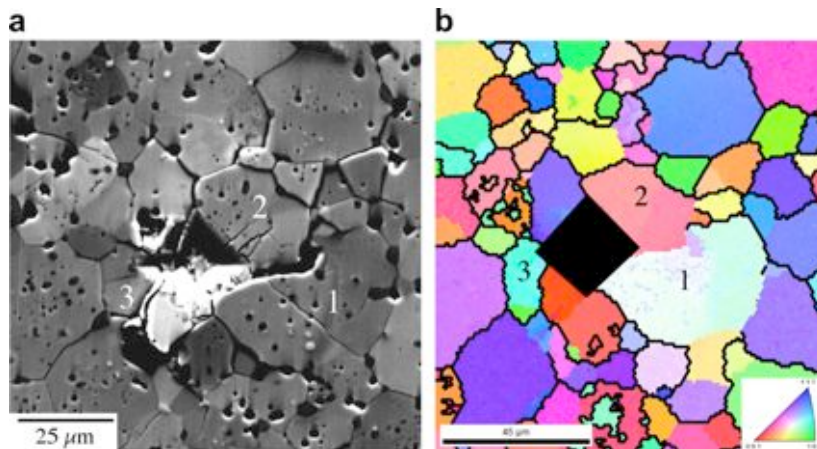
Fig. 10. 'Typical' indent in a sample sintered at 1600 °C in Ar. (a) SEM image and (b) inverse pole figure. The scale bar in (b) is 45 μm long.
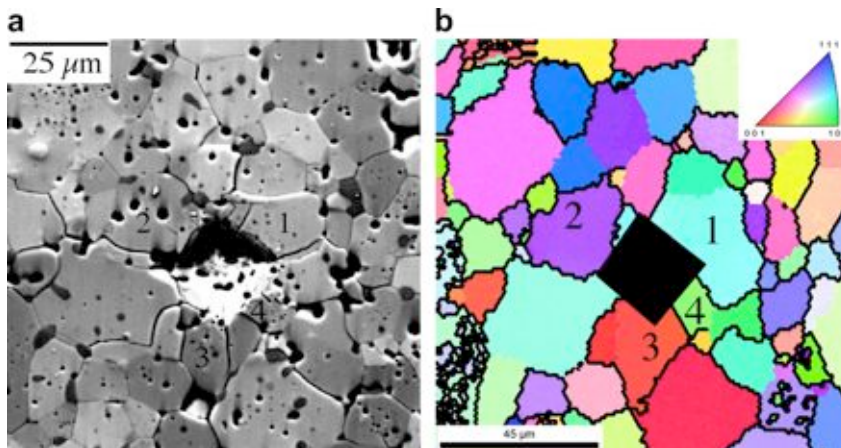

Fig. 11. 'Typical' indent in a sample sintered at 1600 °C in Ar–6% H. (a) SEM image and (b) inverse pole figure. The scale bar in (b) is 45 μm long and thick lines are GB's >30° misorientation angle.

the page) as given by the standard stereographic triangle in the inset of Figs. 10(b) and 11(b). These IPF maps also show the grain boundaries with misorientation angles higher than 30°, as thick black lines. A few grains around the indents are numbered to facilitate their identification. These grains also happen to present transgranular cracks that originate from the corners of the indentation, as would be expected. Note that most of the remaining cracks are intergranular indicating that the grain boundaries, most of which are high angle, are intrinsically weak in ZrN, which is likely to be the case in actinide nitrides as well. This suggests that increasing the fraction of low angle boundaries could lead to improvements in fracture behavior in nitride fuels.

In an effort to identify possible cleavage planes for ZrN the orientation of the traces of the few transgranular cracks observed was measured and the OIM data were used to try to determine if these traces corresponded to low index planes. The angles were measured with respect to the horizontal, and positive values correspond to a counterclockwise rotation. The results are shown in Table 1.

The following low index plane families were used for the match: {0 0 1}, {1 1 0}, {1 1 1}, {0 1 2}, {1 1 2}, and {1 1 3}, chosen because they have low indices [20]. Only those planes with traces that matched the experimental values within 5° are shown. Plane families with more than one value of the calculated trace angle had two or more 'family members' with trace angles within the given tolerance. Results

Table 1
Traces of transgranular cracks around Vickers indents in samples sintered at 1600 °C in Ar or Ar–H

Sample	Grain	Trace angle Θo (observed) (°)	Possible planes	Trace angles Θc (calculated) (°)	$|\Delta\Theta|$ (°)
Ar/1600 °C	1	−34.2	{0 1 2}	−38.2	4.0
			{1 1 3}	−29.0	5.2
Ar/1600 °C	2	57.9	{1 1 2}	59.0	1.1
				60.4	2.5
Ar/1600 °C	2	39.3	{1 1 3}	36.7	2.6
			{0 0 1}	43.0	3.7
Ar/1600 °C	3	10.0	{1 1 2}	9.9	0.1
				11.0	1.0
Ar–H$_2$/1600 °C	1	20.1	{1 1 2}	23.5	3.4
			{0 1 2}	16.2	3.9
				15.7	4.4
Ar–H$_2$/1600 °C	1	60.5	{0 0 1}	59.0	1.5
			{1 1 3}	61.4	0.9
			{1 1 2}	62.5	2.0
			{1 1 1}	65.0	4.5
Ar–H$_2$/1600 °C	2	−5.2	{1 1 1}	−5.0	0.2
Ar–H$_2$/1600 °C	3	93.9	{1 1 2}	93.7	0.2
				88.7	5.2
			{0 1 2}	91.2	2.7
			{1 1 3}	97.6	3.7
Ar–H$_2$/1600 °C	4	−38.4	{1 1 3}	−38.6	0.2
			{1 1 2}	−36.5	1.9
			{0 0 1}	−43.0	4.6

indicate that the crystallographic plane that matched the observed cracks more times was {1 1 2}, followed by {1 1 3}. Further measurements using the same methodology are being performed to collect more statistics, which will allow evaluating the likelihood of fracture along low index planes. Similar measurements will also be carried out in actual fuels, in an effort to establish clear relationships between local crystallography, microstructure and mechanical properties in nuclear fuels.

3.5. Discussion

For the application of sintered ZrN as an inert matrix for transmutation fuels, an open porosity increase will aid in the dissipation of the large amount of helium produced by americium during transmutation. However, increasing open porosity by adding hydrogen to the sintering environment could have adverse effects on the mechanical integrity and longevity of the fuel pellet.

In this study we have noticed that by adding hydrogen to the sintering environment we have noticed list of side effects:

1. A retardation of sample densification for given temperature.

2. A decrease in closed porosity.
3. A small change in the grain misorientation distributions.
4. A subtle but interesting development of a bimodal grain size distribution indicative of pore, bubble or inclusions interacting with the grain boundaries during grain growth.
5. A consistent decrease in hardness.
6. An increase in intergranular cracking.
7. Weaker grain boundaries.

In addition to the above side effects, TEM was performed on a HIPed sample of ZrN in order to try and evaluate the effects hydrogen has on the grain boundary. Fig. 12 is a TEM of a HIPed sample that was heat treated in a N$_2$–6% H$_2$ environment at 1400 °C for 36 h. Note that the diamond shaped voids was not found in the part of the sample that was not heat-treated (TEM not shown). While we are not positive what the formations are at this time, several possibilities exist that involve hydrogen, such as a hydride formation, a pore or a hydrogen bubble that has collapsed allowing the energy of the surrounding crystal structure to dictate the shape of the resulting void rather than the typical spherical shape cause by sufficient internal pressure.
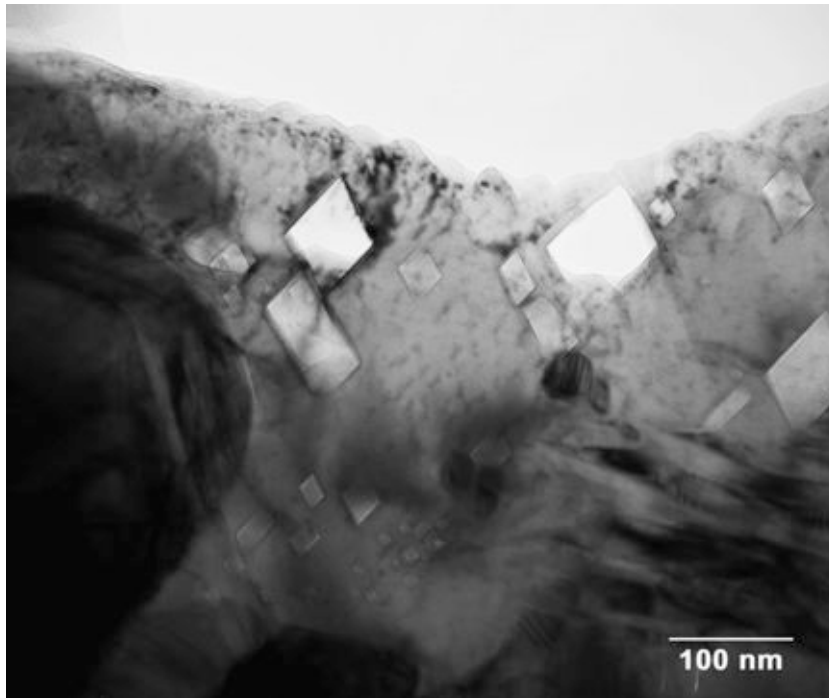
Fig. 12. TEM image of formations found in HIPed ZrN sample after 36 h heat-treatment in N_2–6% H_2 environment at 1400 °C.

Hydrogen is likely to effect the sample's grain growth kinetics due to the negative effect it has on heterogeneous nucleation, by far the most common form of grain nucleation mechanism observed during sintering [17]. Heterogeneous nucleation is induced when surfaces, grain boundaries, second-phase particles and other structural discontinuities serve as favorable nucleation sites. The driving force of such nucleation is the reduction of the surface energy of individual particles. As the material is heated, the surface tension of the particles is reduced, which allows the materials to deform and flow to a more energetically favorable position.

Grain growth relies on available feed material and sufficient temperature. The kinetics of this process indicates that at sufficient temperature grain growth will occur when atoms move from the convex to the concave side of a grain boundary. As the volume of one grain increases, the grain boundary area is increased in order to preserve static equilibrium. As the grain boundary moves it must pull impurities or bubbles that are attracted to the grain boundary [17]. If hydrogen migrates to the surface, or near the surface, of grains during sintering, or hydrides are forming and it is more energetically favorable to have them on the boundaries, then it will take more energy for two adjacent particles to

neck and coalesce if they must displace the inclusions located on the surface. It is possible to now offer an possible explanation for the side effects listed previously.

Gas filled pores and bubbles that are moved by grain boundaries during grain growth can collide and coalesce. However, in samples sintered under hydrogen the motion of closed pores could be reduced by a decrease in grain boundary mobility, due to the increased movement resistance caused by, for example, possible hydride formations and/or hydrogen bubbles on or near grain boundaries. Reduced grain boundary mobility would, in turn, result in a reduction of closed pore formation and a higher open porosity (adjacent particles that have failed to coalesce).

The results of the grain boundary and misorientation angle distributions tend to support the idea that hydrogen could have affected the sintering process through the presence of either hydrogen or hydrides at the grain boundaries. In this sense, high angle boundaries tend to be sites for segregation and precipitation, since they typically have more energy and free volume [19]. The presence of hydrogen (or hydrides) in particular boundaries would tend to 'pin' them, keeping them from moving or changing character, whereas boundaries without these

impurities could move more freely. This can be used to explain the sharper peak of the misorientation angle in the Ar–6% H_2 sample, and the bimodal grain size distribution, since some grains would be able to grow larger than others due to differences in grain boundary mobility.

4. Conclusions

Studies of microstructure and mechanical properties of ZrN sintered under different conditions lead to the following conclusions:

– Using an Ar atmosphere leads to faster sintering and increased grain growth kinetics than those obtained using nitrogen. The microstructures obtained in the Ar atmosphere are similar to those specified for UN in space applications such as nuclear–thermal propulsion and seem to be thermally stable, given the presence of equiaxed grains and pores.
– Lattice parameter measurements indicate that there are structural differences between samples sintered in different atmospheres for a given temperature. It is likely that point defects produced by changes in stoichiometry are playing a role on the kinetics of mass transport during sintering.
– The presence of hydrogen in the sintering environment does not affect the final density significantly; however, it leads to a higher fraction of open porosity, a wider grain size distribution and a tendency to produce a larger fraction of high angle boundaries. This could be due to interactions between either hydrogen or hydrides with the grain boundaries.
– Vickers hardness measurements indicate that the presence of hydrogen leads to lower average values of hardness, which correlate with a larger zone of intergranular cracking around indents. This, in turn, suggests that hydrogen produced grain boundary embrittlement in ZrN.
– High angle grain boundaries are generally weak in ZrN, suggesting that methodologies to increase the fraction of low angle boundaries may be useful to increase the reliability of nitride fuels.

– TEM of HIPed ZrN samples show formations near the grain boundary that are produced with heat-treated in a N_2–6% H_2 environment.
– Local crystallographic orientation data can be used to understand deformation and fracture behavior in nitride fuels and ceramic materials.

Acknowledgement

References

[1] AFCI Program Plan, 2005.
[2] B. Ma, Nuclear Reactor Materials and Applications, Van Nostrand Reinhold Publishing, New York, 1983.
[3] R.B. Matthews, K.M. Chidester, C.W. Hoth, R.E. Mason, R.L. Petty, J. Nucl. Mater. 151 (1988) 334.
[4] B.N. Kiforenko, I.Y. Vasil'ev, Acta Astronaut. 54 (2002) 61.
[5] K. Minato, M. Akabori, M. Takano, Y. Arai, K. Nakajima, A. Itoh, T. Ogawa, J. Nucl. Mater. 320 (2003) 18.
[6] L. Koch, in: Handbook on the Physics and Chemistry of the Actinides, vol. 457, 1986.
[7] Y. Arai, K. Nakajima, J. Nucl. Mater. 281 (2000) 244.
[8] M. Burghartz, G. Ledergerber, H. Hein, R.R.vd. Laan, R.J.M. Konings, J. Nucl. Mater. 288 (2001) 233.
[9] R.J.M. Konings, K. Bakker, J.G. Boshoven, H. Hein, M.E. Huntelaar, R.R.vd. Laan, J. Nucl. Mater. 274 (1999) 84.
[10] M. Streit, F. Ingold, M. Pouchon, L.J. Gauckler, J.P. Ottaviani, J. Nucl. Mater. 319 (2003) 51.
[11] C.T. Walker, G. Nicolaou, J. Nucl. Mater. 218 (1995) 129.
[12] J.C. Spirlet, W. Muller, J. Less-Common Met. 31 (1973) 35.
[13] T. Ogawa, T. Ohmichi, A. Maeda, Y. Arai, Y. Suzuki, J. Alloy. Comp. 224 (1995) 55.
[14] V. Sobolev, S. Lemehov, N. Messaoudi, P.V. Uffelen, H.A. Abderrahim, J. Nucl. Mater. 319 (2003) 131.
[15] D.R. Olander, Fundamental Aspects of Nuclear Fuel Elements, Technical Information Center, Office of Public Affairs, Energy Research and Development Administration, 1976.
[16] J.S. Reed, Principles of Ceramics Processing, Wiley Inter-Science, New York, 1995.
[17] W.D. Kingery, Introduction to Ceramics, John Wiley, New York, 1976.
[18] Data IICfD, PDF# 00-035-0753 (ZrN), 2006.
[19] A.P. Sutton, R.W. Ballufi, Interfaces in Crystalline Materials, Oxford University, New York, 1995.
[20] G.E. Dieter, Mechanical Metallurgy, New York, 1986.

Microwave sintering of 8 mol% yttria–zirconia (8YZ): An inert matrix material for nuclear fuel applications

R.R. Thridandapani [a,*], C.E. Folgar [a], D.C. Folz [a], D.E. Clark [a], K. Wheeler [b], P. Peralta [b]

[a] Department of Materials Science and Engineering, Virginia Polytechnic Institute and State University, Blacksburg, VA 24061, USA
[b] Mechanical and Aerospace Engineering, Arizona State University, P.O. Box 876106, Tempe, AZ 85287, USA

ARTICLE INFO

ABSTRACT

This study focused on reducing overall processing time and temperature for fully stabilized zirconia, an inert matrix material candidate, to minimize the loss of actinides (that will be incorporated into the matrix material), while maintaining at least 90% theoretical density (TD). The effects of different processing routes on bulk density and microstructure were evaluated. The results obtained by adopting microwave sintering for 8 mol% Y_2O_3–ZrO_2 were compared to conventional sintering. A 20 min soak time at 1300 °C resulted in pellets with 90% TD for microwave-processed samples, compared to 77% TD for pellets processed conventionally. A similar density was obtained at lower temperature (1200 °C) by increasing the soak time to 100 min in microwave processing. This time and temperature resulted in 60% TD conventionally processed pellets. Compressive strength values obtained for a 1300 °C (20 min soak time) microwave-processed sample were higher (1600 MPa) as compared to a conventionally processed sample (1300 MPa).

© 2008 Elsevier B.V. All rights reserved.

1. Introduction

Conventional processing of ceramic nuclear fuel involves high-temperature processing of materials, generally above 1600 °C [1]. Due to these processing conditions, it is anticipated that the volatile nature of the actinide-bearing nuclear fuels will result in significant loss of material. The current research aims to process fuel pellets at the lowest possible temperatures in the shortest possible times while maintaining a minimum density of 90% TD, so as to minimize the loss of volatile actinides. This is achieved by adopting a different processing route, i.e., microwave processing. Before giving an overview of microwave processing, a brief background of nuclear fuels is presented. This is followed by experimental procedure, results and discussion.

1.1. Background

Transuranic nuclides (Pu, Np, Am and Cm) are a by-product of nuclear fission reactions [2]. Disposing these long-lived radio nuclides (e.g. [239]Pu with a half-life of 24 000 years and americium ([243]Am) with a half-life of 7360 years) raises questions on the long-term integrity of storage facilities [2–4]. Safe disposal methods have to be sought to isolate these long-lived radioactive materials from the public and to reliably control the inventory so that it cannot be used to produce nuclear weapons.

An alternative to storage is to produce energy by transmuting these highly radioactive nuclides (long-lived) into lighter elements (short-lived) by incorporating them in an inert matrix [5,6]. Inert matrix fuels (IMF) are relatively new fuel designs [7] which provide an option to avoid the fertile reaction by replacing the fertile material with one that is 'relatively' transparent (neutron absorption cross-section <2.7 barns [8]) to neutrons. It is expected that during conventional sintering of IMFs containing Am, the potential for Am evaporation is high. This phenomenon is due to the high vapor pressures exhibited by Am (g) and its oxides (Am_2O_3, AmO (g), AmO_2 (g)) [9,10] under normal sintering conditions. One possible approach to prevent the loss of Am is to adopt microwave processing, which can decrease the overall processing time and temperature.

1.2. Microwave processing

The ability of certain materials to convert the electromagnetic energy into heat makes microwave processing possible [11]. For non-magnetic dielectric materials the electric field in a microwave will polarize the charges. These charges tend to follow the oscillating electric field within the material. The incapability of these charges to follow the continuously altering electric field will lead to the loss of electromagnetic energy within the material. This loss in electromagnetic energy within a material would result in a rise in temperature $\left(\frac{\Delta T}{\Delta t}\right)$ which is given by

* Corresponding author. Tel: +1 540 231 2356; fax: +1 540 231 8919.
  E-mail address: traghu@vt.edu (R.R. Thridandapani).

$$\frac{\Delta T}{\Delta t} = \frac{2\pi f \varepsilon_0 \varepsilon''_{\text{eff}} E^2_{\text{rms}}}{\rho C_p} \left(\frac{{}^\circ C}{\sec}\right), \qquad (1)$$

where $\varepsilon''_{\text{eff}}$ is a unit less quantity that accounts for dielectric losses due to ionic and dipolar reorientation, f is the frequency of the microwave $\left(\frac{1}{\sec}\right)$, ε_0 is the permittivity of free space $\left(8.85 \times 10^{-12} \left(\frac{F}{m}\right)\right)$, E^2_{rms} is the root mean square of the electric field within the material $\left(\frac{V}{m}\right)$, ρ is the bulk density of dielectric material $\left(\frac{\text{kg}}{\text{m}^3}\right)$ and C_p is the specific heat of the material at constant pressure $\left(\frac{J}{\text{kg} \cdot {}^\circ C}\right)$ [12].

Microwave hybrid heating (MHH) is a technique developed to process materials that are low microwave absorbers ($\varepsilon''_{\text{eff}} < 0.08$) at room temperature and show good microwave absorption ($\varepsilon''_{\text{eff}} > 1$) at higher temperatures. In MHH, the initial heating is provided by means of a susceptor. A susceptor is a microwave-absorbing material which supplies heat to the sample (through conduction/convection) until a critical temperature (T_c) is reached. At that point, the sample starts to absorb microwaves and heats independent to the susceptor. In MHH, the sample experiences a combination of both conventional (radiant) heating and microwave heating. This technique may also be used for processing high microwave-absorbing materials, as this technique would provide uniformity in heat distribution within a furnace/oven.

Numerous reports have been cited in the literature on the advantages of MHH over conventional heating [13–19]. For instance, Janney et al. [13] reported a 100–150 °C reduction in sintering temperatures. Goldstein et al. [15] achieved fully sintered samples (5 mol% Y_2O_3–ZrO_2) using MHH at temperatures as low as 1200 °C with a 15–20 min dwell time. Dé [17] reported enhanced results in density, homogeneity in microstructure, and uniformity in mechanical properties for a microwave hybrid sintered Al_2O_3 as compared to a conventionally sintered Al_2O_3.

2. Experimental procedure

2.1. Materials

Commercially available 8 mol% Y_2O_3–stabilized ZrO_2 (8YZ[1]) powders produced through a hydrolysis process in the form of spray dried granules were used for this study. The detailed compositional analysis is shown in Table 1.

2.2. Pellet fabrication

Green pellets (or unfired pellets) were fabricated using uniaxial pressing followed by isostatic pressing. Four grams of as-received powder were poured into a uniaxial mold of 12.5 mm diameter and 70 mm height and subjected to a pressure of 37 MPa. Uniaxially pressed pellets were transferred to isostatic bags and were further subjected to different pressures up to a maximum of 200 MPa.

2.3. Sintering

A commercially available microwave oven[2] (2.45 GHz fixed frequency unit with a maximum power rating of 2100 W) was used for the study. Home model microwave ovens usually have a cavity which supports a large number of resonant modes in a given frequency range. These cavities are also termed as *multimode microwave cavities*. The insulation system for this cavity was built using a refractory material made from aluminosilicate fibers[3] capable of

Table 1
Compositional analysis for 8YZ.

Composition	Mol%
ZrO_2	91.9813
Y_2O_3	7.8385
Al_2O_3	0.0063
SiO_2	0.0065
Fe_2O_3	0.0032
Na_2O	0.1639

withstanding temperatures up to 1700 °C. A susceptor was made by mixing 2 wt% partially stabilized ZrO_2 with 98 wt% Al_2O_3 cement. A desired heating rate of 20 °C/min was maintained by manually switching the power on and off. Temperature measurements for all the sintering runs were monitored using a two-color pyrometer.[4] The field of view of the pyrometer (20 mm) was larger than the sample size (~13.2 mm); therefore, three samples were sintered simultaneously so as to fill in the field of view and avoid any discrepancies with the temperature reading.

The conventional sintering runs were performed in a high-temperature furnace.[5] Temperature measurements for all conventional sintering runs were monitored using an R-type thermocouple. A feedback controller maintained a constant heating rate of ~20 °C/min for all the sintering runs.

2.4. Characterization and testing

The particle size distribution was determined through sieve analysis, particle size analyzer[6] and scanning electron microscope.[7] Scanning electron microscopy (SEM) was also used for imaging the fracture surface of sintered and green samples. Green densities of the samples were calculated from geometric measurements. Bulk densities for the sintered samples were measured using the liquid displacement method according to ASTM C 373. Theoretical density was determined through X-ray diffraction analysis.

Samples for compression testing were harvested from ~9.5 mm diameter disks (4 mm height) that were cut from the pellets using a diamond wafering saw. These disks were quartered using the same saw. These quarters were then ground into small rectangular parallelepipeds (~2.5 mm × 2.5 mm × 2.7 mm) using a 6 μm diamond-impregnated grinding disk followed by 600 grit SiC paper. Uniaxial compression was performed at ambient temperature using a servo-hydraulic load frame[8] with a displacement rate of 0.002 in./min. A custom-made self-aligning fixture was used for testing. Compression testing was also performed at the same displacement rate and with the same fixture at an intermediate temperature (800 °C) in a gettered ultra-high purity argon atmosphere.

3. Results and discussion

3.1. Powder characterization and its compaction behavior

Powder characterization shown in Fig. 1(a)–(c) was performed using SEM imaging, sieve analysis, and particle size analysis, respectively. The SEM imaging of the as-received powder is shown in Fig. 1(a). It can be observed that the starting powders mainly consisted of agglomerates/granules of ~50 μm in size. The inset in Fig. 1(a) shows that the average particle size within the agglomerates was less than 0.5 μm. The results from SEM observations

---

[1] TZ-8Y, Tosoh Corporation, USA.
[2] Panasonic model no. NE 2157R.
[3] Rathboard KVS/400.
[4] Omega, model no. OS3750.
[5] CM bloomerg model no. 0100153.
[6] Horiba model no. LA-950.
[7] LEO (Zeiss) 1550.
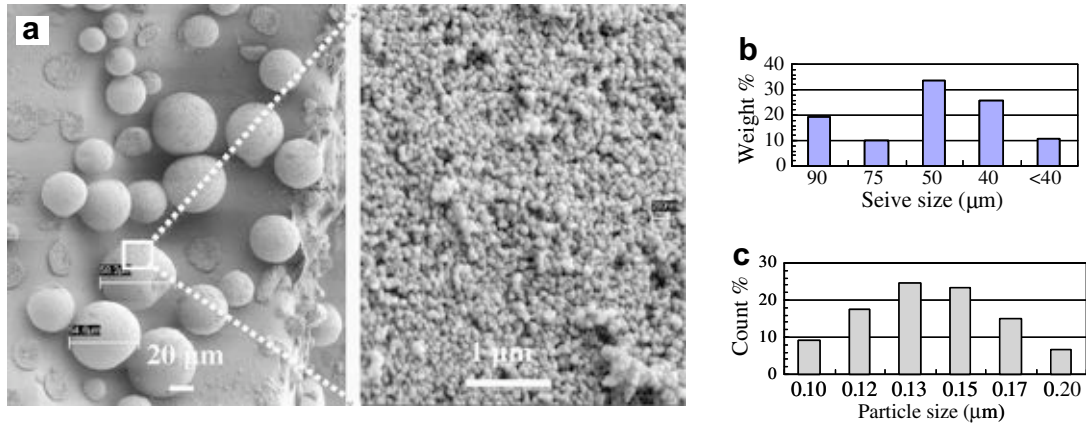[8] Instron 1331.

Fig. 1. (a) SEM imaging of 8YZ powder, and particle size distribution through (b) sieve analysis and (c) particle size analysis.

were confirmed through sieve analysis and particle size analysis. Fig. 1(b) is a plot between the weight fractions of particles on each screen vs. the screen size. As can be seen in Fig. 1(b), the average particle size was ~50 μm. As the lower limit of measurement with sieves was ~20 μm, particle size analysis was used to determine the actual particle size. The results from particle size analysis are shown in Fig. 1(c); it is plot between count fractions of particles vs. the particle size diameter. It shows that the particles within the agglomerates were less than 0.3 μm. This result was used to confirm the SEM observations. It was concluded that particles were in the form of ~50 μm agglomerates during the fabrication of green pellets.

The compaction behavior of these powders can be seen in Fig. 2. There was an increase in green density with increasing pressure (isostatic) from 35 to 200 MPa analysis, and particle size analysis, respectively. Gibson et al. [20] observed a similar behavior for 8YZ powders produced through a co-milling technique. Due to the limitation with the operating pressure in the isostatic press, the green pellets selected for this study were ~46% TD (X-ray calculated as 5.96 g/cc).

3.2. Sintering behavior of 8YZ

3.2.1. Effect of processing technique and temperature on density

Microwave and conventional furnaces were used to study the sintering behavior of 8YZ pellets (shown in Fig. 3). All sintering runs had a constant soak time of 20 min. Fig. 3 is a plot of bulk densities, expressed as a percentage of theoretical density vs. sintering temperature. At low temperatures (i.e., 1100–1300 °C), the densities obtained in microwave-sintered pellets were significantly higher than those achieved in conventionally sintered pellets. At
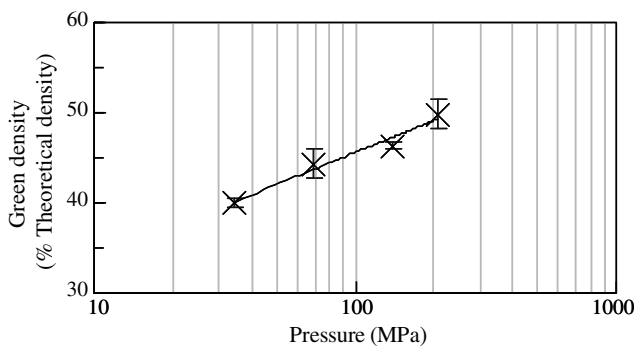
high temperatures (1400 and 1500 °C), the densities obtained for microwave-processed samples were slightly lower when compared to the conventionally processed samples. A significant difference in densities can be seen in 8YZ pellets at a processing temperature of 1300 °C. A value of 91% TD was obtained for the microwave-processed sample as compared to a 77% TD for the conventionally processed sample.

There are differences in density values obtained in this work when compared to the values reported in literature. Janney et al. [13] showed >99% TD for a microwave-sintered 8YZ pellet at 1195 °C. This difference may be attributed to the starting powders and green pellet fabrication. Janney used an isostatic pressure of 210 MPa to fabricate green pellets and prefired the pellets (green) at 1100 °C before subjecting them to microwave sintering. A one-to-one comparison with Janney's results is difficult as the dwell times for the sintering cycle were not the same, i.e., 1 h (Janney's study) vs. 20 min (this study). Samuels and Brandon [18] obtained a similar difference in density values at 1300 °C for a material similar in structure to 8YZ, i.e., 12 mol% Y_2O_3–ZrO_2. They observed ~85% TD for a microwave hybrid sintered sample to ~61% TD for a conventionally sintered sample. A microwave sintering study on 8YZ performed by Nightingale et al. [14] showed a density value of ~89% TD at 1300 °C. Nightingale's value is in close agreement with this work (~91% TD).

Microstructural characterization of pellets processed at 1300 °C was performed via SEM. As a baseline for comparing the microstructural evolution of sintered pellets, SEM imaging was also performed on a green pellet. Fig. 4 contains fractographic images of a green pellet, a conventionally sintered pellet and a microwave-sintered pellet. Individual particles with very little interconnection and grain growth can be clearly seen in Fig. 4b, indicating that
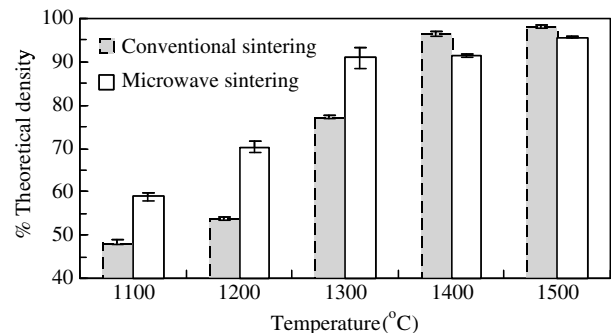

Fig. 2. Effect of isostatic pressure on green density of 8YZ pellets.

Fig. 3. Effect of processing technique and temperature on densification behavior of 8YZ.
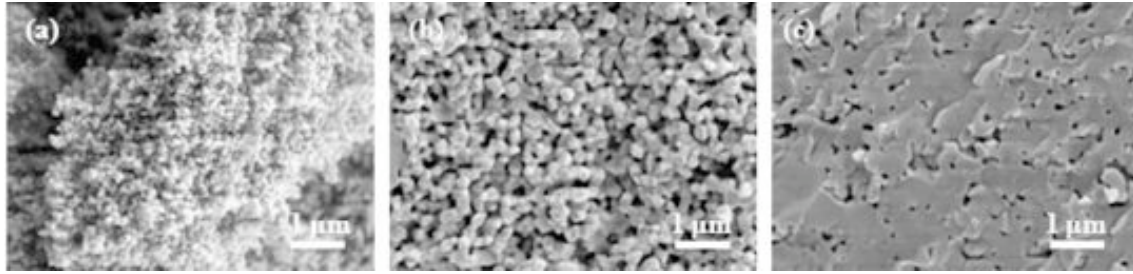
Fig. 4. Fracture surface imaging of (a) a green pellet, (b) a conventionally sintered pellet and (c) a microwave-sintered pellet.

there is less sintering between particles for this sintering profile. Whereas, Fig. 4(c) is an image which shows an enhancement in sintering (i.e., increased particle interconnection, densification and grain growth). From these images, it is clear that the microstructure of the conventionally sintered pellet (Fig. 4(b)) is similar to

its green state (Fig. 4(a)) for this specific set of sintering conditions, unlike the microwave-sintered pellet (Fig. 4(c)) which exhibits more traditional sintering characteristics.

3.2.2. Effect of processing technique and time on density

To further understand the sintering behavior of 8YZ, isothermal sintering experiments were performed at 1200 °C and 1300 °C. Fig. 5(a) and (b) shows the isothermal sintering behavior of 8YZ processed in microwave and conventional furnaces.

At 1200 °C, microwave-processed pellets showed a substantial increase in bulk density from 67% to 90% TD with increase in soak time from 20 to 100 min (Fig. 5(a)). A similar set of experiments performed in a conventional furnace at 1200 °C resulted in a slow increase in density values from 54% to 60% TD (Fig. 5(a)). The rate of increase in bulk density for microwave-processed samples was higher than for conventionally processed samples at 1200 °C. The 8YZ pellets showed very little or no sintering at 1200 °C in a conventional furnace. Isothermal sintering runs performed at 1300 °C (Fig. 5(b)) show that there was no change in density values for microwave-sintered pellets after 20 min as they had achieved their maximum density (~90% TD) for that temperature; whereas, isothermal sintering in a conventional furnace showed a gradual increase in density from 58% to 93% TD with increase in soak time (0–100 min).

As was observed in Fig. 3, temperature had a significant effect on densification for the microwave as well as the conventionally processed samples. The results shown in Fig. 5(a) imply that, at lower temperatures, time (kinetics) has a significant effect on densification for the microwave process than the conventional process. Sintering is a process of bonding particles through heat treatment, resulting in a solid structure. Particle–particle bonding takes place through various types of mass transport mechanisms along the particle–particle interface [21]. These results are indicating that at low temperatures, the mass transport mechanisms responsible for sintering are taking place at a faster rate in a microwave sintering process then in a conventional sintering process.
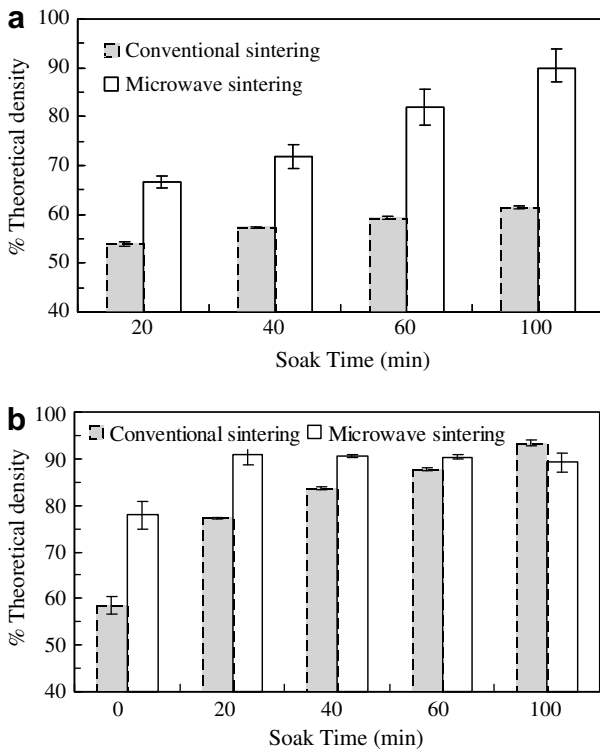

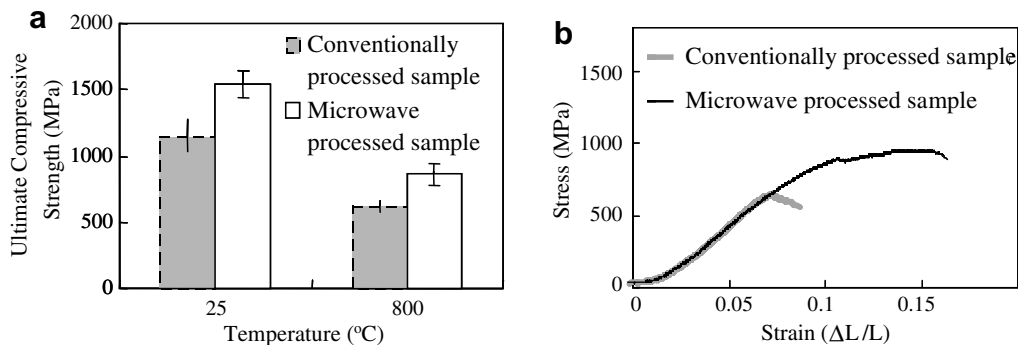**Fig. 5.** Effect of processing technique and time on densification behavior of 8YZ at (a) 1200 °C and (b) 1300 °C.

Fig. 6. (a) Comparison of strength for 8YZ at 25 °C and 800 °C; (b) engineering stress–strain plot at 800 °C.

3.3. Compression testing

Compression testing was performed at both ambient (25 °C) and elevated temperatures (800 °C) in order to evaluate the temperature dependence of the mechanical strength of these materials. Samples sintered at 1300 °C with a soak time of 20 min were selected for the comparative study. The results are presented in Fig. 6.

At both 25 °C and 800 °C (Fig. 6(a)) the microwave-processed samples have a higher compressive strength as compared to the conventionally processed samples. Both sample types exhibit a similar reduction in compressive strength when tested at 800 °C. Fig. 6(b) is the engineering stress and strain plots at 800 °C, and it can be observed that the microwave-sintered samples show an increased capacity for damage tolerance when compared to the conventionally sintered samples. It is possible that the structure of the conventionally sintered sample was not stable enough to withstand the micro-cracking to the same degree as the microwave samples at elevated temperatures. The density difference is undoubtedly a contributing factor to the strength and damage tolerance difference of these two sample types (77% TD conventionally sintered sample vs. 91% TD microwave-sintered sample).

4. Summary

The initial objective for this study was to process materials at lowest possible temperatures in shortest periods of time while achieving at least 90% TD. From the results obtained, it can be concluded that low-temperature processing can be accomplished using MHH. By adopting microwave sintering, 90% TD (in 8YZ) can be obtained at lower temperatures (i.e., 1200 °C with a soak time of 100 min) or in shorter periods of time (i.e., 20 min at 1300 °C). It was also observed that, at 1200 °C, time had a significant effect on the densification process of 8YZ in a microwave process than conventional process. The microwave-processed samples showed a higher compressive strength (1600 MPa) than conventionally processed samples (1300 MPa). Even at higher temperatures (800 °C), the microwave-processed samples showed higher compressive strength and an increased capacity to accumulate damage than the samples processed conventionally.

References

[1] P. Balakrishna, C.K. Asnani, R.M. Kartha, K. Ramachandra, K.S. Babu, V. Ravichandran, B.N. Murty, C. Ganguly, Nucl. Technol. 127 (1999) 375.
[2] D. Westlén, Prog. Nucl. Energy 49 (2007) 597.
[3] F.N.V. Hippel, Nature 394 (1998) 415.
[4] R.C. Ewing, Proc. Natl. Acad. Sci. 96 (1999) 3432.
[5] R.J.M. Konings, D. Haas, C. R. Phys. 3 (2002) 1013.
[6] V. Artisyuk, M. Saito, A. Stankovsky, Prog. Nucl. Energy 47 (2005) 327.
[7] C. Degueldre, J.M. Paratte, J. Nucl. Mater. 274 (1999) 1.
[8] M. Burghartz, H. Matzke, C. Léger, G. Vambenepe, M. Rome, J. Alloys Compd. 271 (1998) 544.
[9] T.B. Lindemer, Oak Ridge National Laboratory, ORNL/TM-2002/133, 2002.
[10] J.J. Moore, ANS/ENS Int. Meeting and Nucl. Technol. Expo., 2007.
[11] J.D. Katz, Ann. Rev. Mater. Sci. 22 (1992) 153.
[12] D.E. Clark, D.C. Folz, What is microwave processing?, in: D.E. Clark, D.C. Folz, C.E. Folgar, M.M. Mahmoud (Eds.), Microwave Solutions for Ceramic Engineers, J. Am. Ceram. Soc., Ohio, 2005, pp. 1–35.
[13] M.A. Janney, C.L. Calhoun, H.D. Kimrey, J. Am. Ceram. Soc. 75 (1992) 341.
[14] S.A. Nightingale, H.K. Worner, D.P. Dunne, J. Am. Ceram. Soc. 80 (1997) 394.
[15] A. Goldstein, L. Giffman, S. Barziv, J. Mater. Sci. Lett. 17 (1998) 977.
[16] K.H. Brosnan, G.L. Messing, D.K. Agarwal, J. Am. Ceram. Soc. 86 (2003) 1307.
[17] A. Dé, MS thesis, University of Florida, 1990.
[18] J. Samuels, J.R. Brandon, J. Mater. Sci. 27 (1992) 3259.
[19] J.M. Moore, PhD dissertation, University of Florida, 1999.
[20] I.R. Gibson, G.P. Dransfield, J.T.S. Irvine, J. Mater. Sci. 33 (1998) 4297.
[21] R.M. German, Sintering Theory and Practice, John Wiley, New York, 1996.